2010

Calibration of the UMass Advanced Multi-Frequency Radar

Matthew Mclinden
University of Massachusetts Amherst

CALIBRATION OF THE UMASS ADVANCED MULTI-FREQUENCY RADAR

A Thesis Presented

by

MATTHEW L. MCLINDEN

Submitted to the Graduate School of the
University of Massachusetts Amherst in partial fulfillment
of the requirements for the degree of

MASTER OF SCIENCE IN ELECTRICAL AND COMPUTER ENGINEERING

February 2010

Electrical and Computer Engineering

CALIBRATION OF THE UMASS ADVANCED MULTI-FREQUENCY RADAR

A Thesis Presented

by

MATTHEW L. MCLINDEN

Approved as to style and content by:

Paul R. Siqueira, Chair

Stephen J. Frasier, Member

Dennis L. Goeckel, Member

Christopher V. Hollot, Department Chair
Electrical and Computer Engineering

For my Mom.

ACKNOWLEDGMENTS

While my name is on the cover of this document, I am constantly mindful that the accomplishments here belong to a community of people, both inside the Microwave Remote Sensing Lab and out.

Professor Paul Siqueira provided constant support and guidance to me as I began the transformation from undergrad to researcher. I am grateful for the trust he gave me. Nino Majurek, with his extensive experience in this work, was always available to take a phone call to point me in the right direction. My other professors, including Dr. Goeckel, Dr. Hollot, and Dr. Frasier, changed the way that I think about the world through their classes and conversations.

It is the community at MIRSL that truly make it special. Harish with his optimistic enthusiasm, Vijay for the late-night coffee and company, Ivona for her grasp of the big picture, Razi for his humor, Pei for loaning me courage to work on the system, and Krzysiek for his guitar playing and parties.

My graduate studies at UMass would not have been possible without the support of Cathy Long and Terence Doiron, my branch heads in the Microwave Instrument Technology Branch at NASA/GSFC. They stood by me as I extended my co-op position to the larger half of a decade through years of undergraduate and graduate education. Paul Racette, my mentor at Goddard, was always someone I could turn to for advice. Jared and Kevin gave me the push I needed to finally get this document Written. I also want to thank Bob Meneghini for his help in the final months of work. he graciously took the time to discuss my results and to provide direction for further study any time I needed a hand with the scientific work in this document.

Most of all, I want to thank my parents for believing in me. In all the work I have done, I have been able to sleep easier knowing that I had their support whatever the outcome.

ABSTRACT

CALIBRATION OF THE UMASS ADVANCED MULTI-FREQUENCY RADAR

FEBRUARY 2010

MATTHEW L. MCLINDEN

B.Sc, UNIVERSITY OF MASSACHUSETTS

M.S.E.C.E., UNIVERSITY OF MASSACHUSETTS AMHERST

Directed by: Professor Paul R. Siqueira

The Advanced Multi-Frequency Radar is a three-frequency system designed and built by the University of Massachusetts Microwave Remote Sensing Lab (MIRSL). The radar has three frequencies, Ku-band (13.4 GHz), Ka-band (35.6 GHz), and W-band (94.92GHz). The additional information gained from additional frequencies allows the system to be sensitive to a wide range of atmospheric and precipitation particle sizes, while increasing the ability to derive particle microphysics from radar retrievals.

This thesis details the calibration of data from the Canadian CloudSat/CALIPSO Validation Project (C3VP) held during January 2007 in Ontario, Canada. The calibration used internal calibration path data and was confirmed through comparison of precipitation reflectivity with an Environment Canada radar.

The calibrated data was then used to estimate the median mass diameter of precipitating snow from a high-priority C3VP data set. This median mass diameter retrieval

was compared to the results from a local ground instrument, the Snow Video Imager (SVI), showing good agreement.

TABLE OF CONTENTS

LIST OF TABLES

Table **Page**

LIST OF FIGURES

Figure **Page**

CHAPTER 1

INTRODUCTION

1.1 History and Motivation

AMFR, or the *Advanced Multi-Frequency Radar*, was developed by the University of Massachusetts Microwave Remote Sensing Lab (MIRSL) under a grant by the National Science Foundation. It was designed as a replacement and upgrade to the *UMass Cloud Profiling Radar System* (CPRS). The upgraded AMFR system features properties to make it uniquely capable of producing information on cloud and precipitation microphysics by combining three frequencies in a polarimetric radar. The CPRS instrument had Ka- and W-band channels co-locaded by the same antenna, but not matched in volume. AMFR includes beams with matched volumes and a third lower frequency for measurements that are less attenuated by precipitation.

AMFR's Ku-band channel experiences less attenuation and is more sensitive to larger particles than the higher frequencies. This frequency also provides AMFR with channels to match the upcoming NASA *Global Precipitation Measurement* (GPM) mission's *Dual-frequency Precipitation Radar* (DPR). This upcoming satellite mission is expected to produce wide-spread and valuable information on precipitation over most of the world, and will feature a Ku- and Ka-band radar in addition to a multiple-frequency millimeter-wave radiometer.

As the GPM DPR will be the first radar of its kind in space, the ground information provided by AMFR could be very valuable for both algorithm development and validation for the satellite's science data.

1.2 Thesis Contents

The work documented in this thesis covers the transformation of uncalibrated data into calibrated radar products and dual-wavelength cloud and precipitation microphysics retrievals. The scientific results shown are one of the first examples of dual-wavelength snow-size distribution retrievals with concurrent in-situ data.

Chapter 2 provides a qualitative description of active microwave remote sensing of weather. Specific topics include reflectivity, dual-wavelength measurements, and drop-size distributions. This chapter will provide the background necessary for the remainder of the document.

Chapter 3 describes the AMFR system. It provides information on the physical structure, RF and IF electronics, and data system. It also details the methods used to retrieve the radar products used for cloud and precipitation microphysics research.

Chapter 4 discusses the method used to calibrate AMFR following the *Canadian CLoudSat/CALIPSO Validation Project* (C3VP) experiment in 2007. It describes the conversion from the received power to reflectivity measurements, associated errors, and the combining of multiple pulse lengths into a single image.

Chapter 5 details AMFR's first field experiment, C3VP. The system experienced some difficulties associated with the severe weather. These problems are largely overcome, leading to a demonstration of successful calibration of C3VP data through comparison with an Environment Canada radar.

Chapter 6 shows the transformation of C3VP data into precipitation microphysics information. While previous work with this data is shown in [4] was largely dedicated to using raw data and doppler products, this analysis focuses on dual-wavelength ration measurements. This chapter shows the successful retrieval of snow-size distribution data as confirmed by the measurements simultaneously taken by a ground-based video instrument called the Snow Video Imager.

CHAPTER 2

RADAR METEOROLOGY

This chapter introduces weather radar products and their importance to weather forecasting and climate research. It describes both single- and multi-frequency radar products and shows the scientific motivation behind the AMFR effort.

2.1 Electromagnetic Scattering and Propagation

As radars by definition measure the electromagnetic waves scattered from a transmitted signal, it is necessary to have a way of describing how a scattered wave relates to an incident wave based on the scatterer in question. The scattering matrix $[S]$ is one way to fully describe the backscatter of a transmitted wave of arbitrary polarization, and relates the electric field scattered from a volume to the incident field, as in

$$\begin{bmatrix} E_h^s \\ E_v^s \end{bmatrix} = [S] \begin{bmatrix} E_h^i \\ E_v^i \end{bmatrix}. \tag{2.1}$$

The scattering matrix is defined as

$$[S] = \begin{bmatrix} S_{hh} & S_{hv} \\ S_{vh} & S_{vv} \end{bmatrix} \tag{2.2}$$

where S_{ab} is the complex reflection at polarization a from polarization b, shown as

$$S_{ab} = |S_{ab}| \, e^{j\delta_{ab}} \tag{2.3}$$

where δ_{ab} is the change in phase (radians). This uses the forward-scattering assumption as described in [1].

Not all of the elements of the scattering matrix are useful in practice, or even independent. Precipitation is nonmagnetic so the cross-polarizations in the scattering matrix are reciprocal. As such, $|S_{hv}| = |S_{vh}|$ and $\delta_{hv} = -\delta_{vh}$. Additionally, the absolute phase of any single parameter is not useful in practice as the measurement volume typically spans many wavelengths, so any absolute phase signature is dominated by the phase changes associated with the range to the individual scatterers [1]. Only the differences in phase between different elements of the scattering matrix are useful, leading to the *relative phase* version of the scattering matrix

$$[S] = e^{j\delta_{hh}} \begin{bmatrix} |S_{hh}| & |S_{hv}|\, e^{j(\delta_{hv}-\delta_{hh})} \\ |S_{vh}|\, e^{j(\delta_{vh}-\delta_{hh})} & |S_{vv}|\, e^{j(\delta_{vv}-\delta_{hh})} \end{bmatrix}. \tag{2.4}$$

The scattering matrix alone is not sufficient to describe a radar return from a particular volume. A signal will also be altered during propagation due to particles and vapor in the medium. These effects can also behave differently for different polarizations depending on the medium, and are described by the transmission matrix $[T]$ where

$$\begin{bmatrix} E_h(z) \\ E_v(z) \end{bmatrix} = [T] \begin{bmatrix} E_h(0) \\ E_v(0) \end{bmatrix}. \tag{2.5}$$

In (2.5), $E(0)$ is the wave at position $z = 0$ and $E(z)$ is the wave at position z. The transmission matrix $[T]$ describes the changes in the wave over that distance, and is given by

$$[T] = \begin{bmatrix} T_h & 0 \\ 0 & T_v \end{bmatrix} = \begin{bmatrix} e^{-jk^h_{\text{eff}}z} & 0 \\ 0 & e^{-jk^v_{\text{eff}}z} \end{bmatrix} \tag{2.6}$$

where z is the position and k^h_{eff} is the effective wave number of the propagation medium at polarization h. Equation 2.6 also assumes that the fields originating in one

polarization do not coherently couple into the other, and therefore off-diagnoal terms in the expression are zero. The non-zero values of (2.6) are complex, and describe both the attenuation and the change in phase that the coherent field experiences as it passes through the intervening medium. The combined effects of the propagation media and the scattering can be shown as

$$\begin{bmatrix} E_h^r \\ E_v^r \end{bmatrix} = \begin{bmatrix} T_h & 0 \\ 0 & T_v \end{bmatrix} \begin{bmatrix} S_{hh} & S_{hv} \\ S_{vh} & S_{vv} \end{bmatrix} \begin{bmatrix} T_h & 0 \\ 0 & T_v \end{bmatrix} \begin{bmatrix} E_h^i \\ E_v^i \end{bmatrix}. \tag{2.7}$$

This chapter will discuss the commonly used radar products, how they fit into the relative phase scattering matrix and transmission matrix, and techniques used to derive them.

2.2 Radar Cross Section and Volume Reflectivity

The Radar Cross Section (RCS) is a product that shows the reflected power as compared to the transmitted power of a wave. If a measured target reflects a portion of the incident power in the beam back at the receiver, the RCS is the size that a hypothetical target that scattered all incident power equally in all directions would have to be to reflect the same power back to the radar.

The backscatter can be measured in any polarization, and can be related to the scattering matrix shown in (2.4) by

$$\sigma_{h/v} = 4\pi \left| S_{hh/vv} \right|^2 \tag{2.8}$$

for a single scatterer at polarization h. The backscatter σ is measured in units of m^2.

The radar cross section is defined for a single scatterer, and is primarily used for non-weather radars. Weather radars typically measure many scatterers in a volume, so instead use volume reflectivity, defined as

$$\eta = \frac{1}{V} \sum_{i=1}^{N} \sigma_i. \tag{2.9}$$

In the above, V is the measured volume in m^3, and N represents the total umber of reflectors in the volume. The resulting volume reflectivity η is measured in m^2/m^3. Equation 2.9 assumes that the phases of the individual reflections are independent, allowing the power to be summed directly. This is a reasonable assumption with randomly distributed scatterers in a volume hat spans many wavelengths. With multiple scatterers in the measurement volume, the assumption behind (2.8) is no loner valid, and the volume reflectivity can be polarized and related to the scattering matrix of the volume through

$$\eta_h = \frac{4\pi \left|S_{hh}\right|^2}{V}. \tag{2.10}$$

2.3 Scattering From a Dielectric Sphere

The first comprehensive analysis of electromagnetic scattering from small dielectric spheres was published by Gustav Mie in 1908. The resulting equations are quite complex, and are not detailed here, however the backscatter from a water sphere is shown in Figure 2.1.

In Figure 2.1, two of the three regimes of electromagnetic scattering can be seen. For small particles, the backscatter is predictable through a simple power relationship including the wavelength and particle diameter. This is termed the Rayleigh regime. For larger particles with a diameter on the order of a wavelength, the backscatter changes rapidly as reflections from different parts of the individual particles add in and out of phase. This is known as the Mie regime, so named after Gustav Mie. Finally the optical regime covers particles with diameters much larger than a wavelength, and the normalized RCS becomes flat with respect to diameter, indicating that the reflected power is proportional to the projected surface of the particle into the direction of propagation.

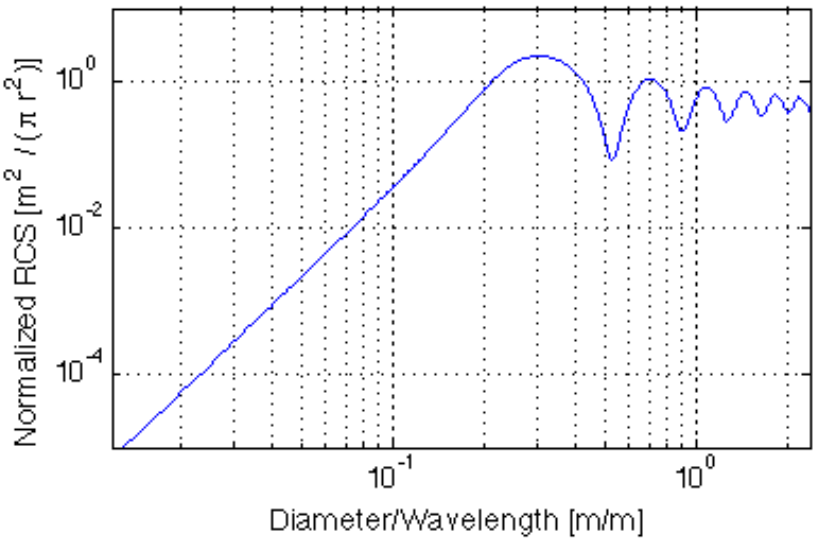

Figure 2.1: Normalized radar cross section of a single sphere of water as a function of drop diameter

The easiest regime to work with is the Rayleigh regime. For diameters much smaller than a wavelength the radar cross section of an individual scatterer can be approximated as

$$\sigma = \frac{\pi^5}{\lambda^4}|K|^2 D^6 \tag{2.11}$$

where σ is the radar cross section in $[m^2]$, λ is the wavelength in meters, and D is the diameter of the particle in meters. The factor K in (2.11 is related to the material properties of the scatterer, and is given by

$$K = \frac{n-1}{n+2} \tag{2.12}$$

where n is the complex index of refraction given by

$$n = \sqrt{\epsilon_r}. \tag{2.13}$$

Assuming all reflectors in a volume exist in the Rayleigh regime, (2.11) and (2.9) can be combined to provide the volume reflectivity of the volume,

$$\eta = \frac{1}{V} \sum_{i=1}^{N} \frac{\pi^5}{\lambda^4} |K|^2 D_i^6 \tag{2.14}$$

in m^2/m^3.

The Rayleigh scattering approximation does not always hold true for higher radar frequencies for precipitation associated with typical weather phenomena. Ku-band radars will experience some effects from Mie scattering, and the Ka- and W-bands will fall into the Mie regime regularly. This difference in the radar cross section of larger particles between frequencies is the foundation of the multi-frequency measurements made in this thesis.

2.4 Reflectivity Factor

Different frequency radars have different advantages in terms of spacial resolution, sensitivity, and cost. As such, a common "language" was needed to tie data from these different radars together. In (2.11), the log of backscattered power for Rayleigh scatterers varies with the fourth power of the wavelength. This allows a common unit of measurement over a wide range of frequencies so long as the assumptions required for Rayleigh reflectivity are met. The resulting standard for reporting meteorological radar data is the unit "Z" where

$$Z = \frac{1}{\Delta V} \sum D_i^6. \tag{2.15}$$

The volume is typically measured in meters, while the particle diameter is typically measured in millimeters. For instance, one drop one millimeter in diameter per cubic meter would lead to a Z of unity. Using Z as a common unit ensures that the volume and frequency differences between radars are largely accounted for so long as the scatterer remains in the Rayleigh regime and the material characteristics do not change.

As Z is the combination of reflections from all particles in a volume, combinations of different drops of different sizes may lead to identical Z products. This is where good estimates of the drop-size distribution are necessary to determine the true volume of reflectors in the measurement.

The conversion from volume reflectivity to Z is a linear scaling derived from(2.15) and (2.14), expressed as

$$Z = \frac{\lambda^4}{\pi^5 |K|^2} \eta 10^{18}. \tag{2.16}$$

The range of typical Z values cover many octaves, so Z is typically expressed in decibels as "dBZ". The 10^{18} factor comes from the use of mm for the drop diameter while the diameter in (2.14) is given in meters.

In practice there are difficulties using Z as a common standard. For instance, while water is used as the dielectric for K, actual precipitation is often in the form of ice or aggregated ice (snow). Even when dealing with liquid precipitation, K will vary with both frequency and temperature. Additionally, the Rayleigh approximation on which the reflectivity factor is based breaks down for mid- and high-frequency radars, as the reflectors move from the Rayleigh to the Mie regime.

Due to these common factors that regularly invalidate the reflectivity factor assumptions, measurements are often expressed as the *equivalent reflectivity factor* or $dBZe$. The equivalent reflectivity factor is what the observed reflectivity factor would be even should the associated assumptions in material property and size not hold. Figure 2.2 shows the equivalent reflectivities of a single water drop per cubic meter at Ku- and Ka-bands. The agreement of the two frequencies in the Rayleigh regimes is clearly visible, as is the breakdown of the Rayleigh approximation in the Mie regime. The definition for Z as given by (2.15) follows the Rayleigh approximation shown by the black dashed line.

The reflections resulting in radar measurements are caused by discontinuities. Since rain has a larger dielectric constant compared to air than does snow, it is

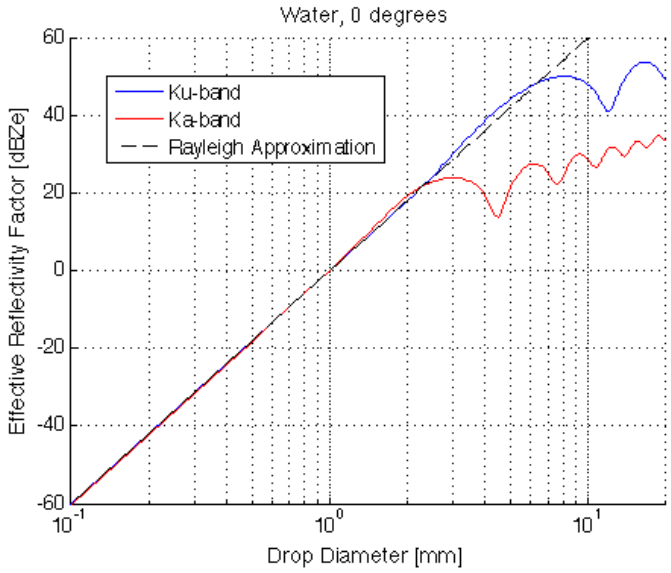

Figure 2.2: Equivalent reflectivity factor for one spherical drop of water per cubic meter at Ku- and Ka-bands. The Rayleigh approximation (and the actual dBZ by definition) is also shown.

predictable that snow would have a far weaker equivalent reflectivity factor than a similar volume of rain. Figure 2.3 shows the equivalent reflectivity factor of a single snowflake per cubic meter, calculated for dry snow with a mass of 0.05 grams per cubic centimeter. The scale of Figure 2.3 is the same as in Figure 2.2. This calculation uses the spherical flake approximation and a dielectric constant computed using the method given in [11].

Despite the limitations associated with dBZe, it is the most common unit for representing weather radar data of all types of precipitation. The advantage lies in that data can be immediately understood to some extent without knowledge of the specifics of the radar in question. The drawback is that particular care must be taken in understanding the assumptions that were made in generating the volume reflectivity to reflectivity factor conversion when working quantitatively with data.

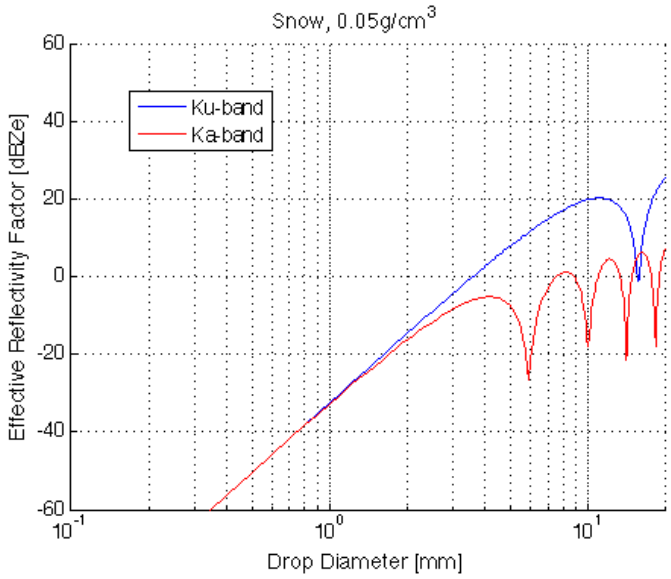

Figure 2.3: Equivalent reflectivity factor for spherical snow flake per cubic meter at Ku- and Ka-bands. The scale is the same as Figure 2.2.

2.5 Drop-Size Distribution

The above section on electromagnetic scattering addresses the power reflected from a single target. In practice, weather radars measure the net effect of many such small particles in a larger volume. As such, the reflected signal is the sum of many independent reflections of different sizes and positions.

It is useful, therefore, to have models of particle-size distributions common to different types of weather phenomena. An accurate model allows for the ratio of received to transmitted power from a to lead directly to an estimation of the amount of water or ice in the volume. The most famous Drop-Size Distribution (DSD) is a two-parameter distribution introduced by Marshall and Palmer in 1948 based on empirical data. The Marshall-Palmer distribution is a special case of the exponential distribution

$$N_{exp}(D) = N_0 exp(-\Lambda D) \tag{2.17}$$

where D is the diameter of particles, N_0 controls the intensity, and Λ is used to control the shape of the distribution. For the Marshall-Palmer distribution, N_0 is $8000mm^{-1}m^{-3}$, and $\Lambda = 41R^{-0.21}cm^{-1}$ where R is the rain rate in mm/hour [5].

A second commonly used distribution is the Gamma distribution, given by

$$N_\Gamma(D) = N_0 D^\mu exp\left(\frac{-(3.67+\mu)D}{D_0}\right) \tag{2.18}$$

where μ is a parameter that is used to to adjust the shape of the distribution. D_0 is the *median mass diameter*, defined where

$$2\int_0^{D_0} D^3 N(D)\, dD = \int_0^\infty D^3 N(D)\, dD. \tag{2.19}$$

This distribution was proposed in 1983 by C. W. Ulbrich in [13] as a way of expanding the existing models to be more flexible in terms of precipitation and storm type. This model uses three parameters rather than two for controlling the shape of the distribution, and is the distribution used in the analysis found in Chapter 6.

An interesting property of drop size distributions is the dependence of the backscatter on larger particles in the Rayleigh regime. As can be seen in (2.11, the backscatter of particles in the Rayleigh regime increase with the diameter to the sixth power, while the volume increases with the diameter to the third power. The result is that the importance of the larger particles of the drop-size distribution is inflated compared to the mid- and small-diameter ranges. Hence the tails of the distribution, which are related to larger particle sizes, have a great impact on the backscattered power. The Gamma distribution is shown in Figure 2.4. Also shown in Figure 2.4 are the relative weighting of the distribution in both mass and Rayleigh reflectivity.

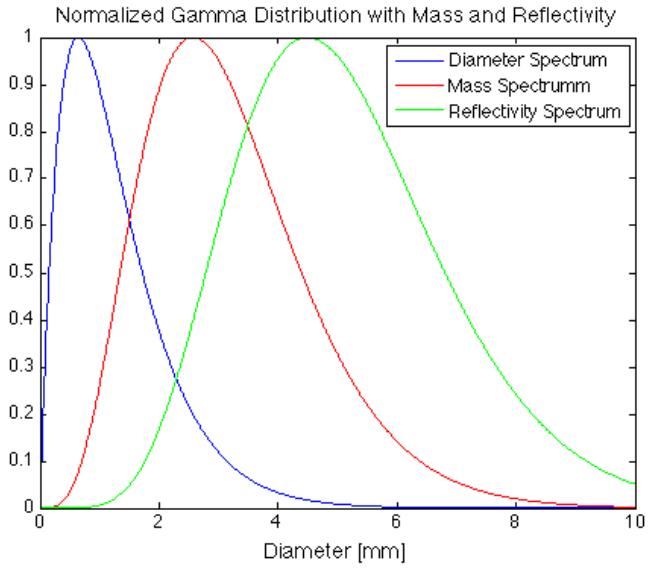

Figure 2.4: A Gamma drop-size distribution ($D_0 = 1mm$, $\mu = 1$) with the corresponding volume and Rayleigh backscatter contributions, all normalized to a maximum of one

2.6 Doppler Velocity

The Doppler effect is a change in frequency of a scattered or reflected wave due to the radial velocity of the reflector. It is impractical for pulsed weather radars to measure this minute effect directly, however "Doppler" radars routinely measure the mean velocity of weather systems through comparing the phase of successive pulses.

Consider a reflector with mean velocity u and a radar with PRF $1/T_s$ that pulses at times nT_s where n is the set of real integers. The position of that reflector at all times t would be $R(t) = R_0 + t\,u$ where R_0 is the position of the scatterer at $t = 0$. The contribution to the received phase due to the distance to the target of each pulse would be

$$S_n = e^{-j2k(R_o + nT_s u)}. \tag{2.20}$$

The product of S_n and the complex conjugate of S_{n+1} leaves

$$S_n S_{n+1}^* = e^{j2kT_s u}. \tag{2.21}$$

Taking the angle of this result

$$\Delta\phi = \angle(e^{j2kT_s u}) = 2kT_s u \tag{2.22}$$

and solving for the velocity u produces the classical equation for pulsed doppler radar

$$u = \frac{\Delta\phi}{2kT_s} = \frac{\lambda\Delta\phi}{4\pi T_s}. \tag{2.23}$$

It is important to note that the Doppler results will "fold" every 2π radians. Thus, the maximum velocity that a pulsed Doppler radar can measure without ambiguity is

$$u_{max} = \pm\frac{\lambda}{4T_s}. \tag{2.24}$$

Some radars use multiple PRFs to allow for better "unfolding" of the Doppler results. For a multiple-frequency radar such as AMFR this is not necessary as the different frequencies will have different wavelengths, and thus different folding velocities.

2.7 Multiple Polarization Products

The parameters above all involve either a single polarization, or are independent of polarization. It is possible, with dual-polarized receivers and transmitters, to fill out the full scattering matrix shown in (2.2). Although it is rare that radars fully populate the scattering matrix, there are some common polarimetric products that provide information about precipitation type and shape.

2.7.1 Polarimetric Radar Types

There are three common, but not mutually exclusive, approaches to populating the scattering matrix. For simplicity, it will be assumed here that all approaches use vertical (v) and horizontal (h) polarizations, although other polarization can also be used.

The first method is a radar that transmits a single polarization, but receives both polarizations. It is possible for a radar of this design to gather information on either the left or right side of the scattering matrix. The advantage of this method is the reduced complexity of the transmitter, which tends to be the bulk of the cost of building a radar.

The second common method is a *simultaneous-transmit* radar, which emits both h and v simultaneously (equivalently, this is a 45 degree or circularly polarized wave depending on phase). This allows for good measurement of the relative phase between the polarizations ($\delta_{vv} - \delta_{hh}$), however the method couples the cross-polarization reflections in with the much larger co-polarization, making it impossible to obtain information in the top-right and bottom-left elements of the scattering matrix. A radar of this type has the added complexity of requiring a power splitter in the transmit path or matched transmitters for h and v.

The final common type is the *polarization-diversity* radar, which transmits h and v separately while always receiving both polarizations. This allows for good estimations of the magnitudes in the scattering matrix, but as the phase elements are defined at zero time-lag, they cannot be directly measured with this type of radar. Some methods allow for this weakness to be partially corrected for (as will be shown), however they are not possible in all cases. The advantage of this method is a more complete filling of the scattering matrix, however it requires either multiple transmitters or active switching in the transmit path. As a result, this tends to be a more expensive option.

It is quite possible for radars to be built to transmit in both polarization-diversity and simultaneous-transmit modes, however this is rarely done due to the high cost of such a transmitter. AMFR is a polarization-diversity radar.

2.7.2 Differential Reflectivity and Linear Depolarization Ratio

Differential Reflectivity (Z_{dr}) is the measure of the log of the ratio of the magnitude of horizontal reflections and the magnitude of vertical reflections in a media, or

$$Z_{dr} = 10log_{10}\left(\frac{\left\langle |S_{hh}|^2 \right\rangle}{\left\langle |S_{vv}|^2 \right\rangle}\right). \tag{2.25}$$

Like other polarimetric parameters, differential reflectivity gives an indication of the shape of reflectors in the measurement volume. In the particular case of rain, drops of liquid water flatten as they fall, becoming longer in the horizontal plane than the vertical plane. This results in higher horizontal reflectivity.

As large drops flatten more than small drops, Z_{dr} can be used as an indicator of drop-size distribution, although in recent years differential phase has been used more commonly for this purpose. Differential Reflectivity is useful for detecting the presence of hail in heavy rain. As hail will not flatten due to falling its differential reflectivity will be near zero. Additionally, due to hail's large size it will tend to dominate a reflectivity measurement, thus making the Z_{dr} of heavy rain with hail be near zero despite the presence of flattened raindrops.

The Linear Depolarization Ratio (LDR) is a measure of how a volume rotates reflected waves, and is given by

$$LDR = 10log_{10}\left(\frac{\left\langle |S_{vh}|^2 \right\rangle}{\left\langle |S_{hh}|^2 \right\rangle}\right). \tag{2.26}$$

As simultaneous transmit radars are unable to separate the cross-polarization elements of the $[S]$ matrix from the co-pol elements, they are unable to measure LDR.

2.7.3 Specific Differential Phase

The specific differential phase K_{dp} is, unlike previous parameters listed, a measure of the effects of the transmission matrix. It is defined as

$$K_{dp} = \frac{\delta \Phi_{DP}(r)}{\delta r[m]} 10^3 \tag{2.27}$$

where r is the range of the volume in question (in meters) and $\Phi_{dp}(r)$ is the differential phase in degrees per kilometer, or the difference in phase between the horizontal and vertical waves at range r. The differential phase is shown as

$$\Phi_{dp}(r) = 2\left[\angle T_h(r) - \angle T_v(r)\right] + \Phi_{ds} = 2\,\Re\Big(k^h_{\text{eff}} - k^v_{\text{eff}}\Big)\frac{180}{\pi} + \Phi_{ds} \tag{2.28}$$

where T and k_{eff} are taken from the transmission matrix shown in (2.6) and Φ_{ds} is the differential phase introduced by the scattering of the target. In a volume of many randomly distributed reflectors, such as clouds or precipitation, the expected value of Φ_{ds} is zero.

During propagation, particles that interact strongly with a particular polarization will retard the propagation of that component of the electromagnetic field. As such, measuring the difference in phase between the radar returns of two polarizations over space gives an indication of particle shape.

In radar meteorology, the specific differential phase is regularly used to provide information about attenuation and precipitation type. Unlike differential reflectivity, K_{dp} is a phase measurement and is less effected by attenuation or calibration errors.

2.8 Multiple-Frequency Products

Multiple-frequency products are a more recent avenue of research for radar meteorology due to the expense and complexity associated with building and maintaining

multiple independent transmitter, receiver, and antenna subsystems in the same system. The two most common multiple-frequency products are the *dual-wavelength ratio* or *DWR*. This is also regularly referred to as the *dual-frequency ratio* or *DFR*). The use of doppler measurements, or *dual-doppler* is also mentioned, however that avenue of research was not explored in this work.

2.8.1 Dual-Wavelength Ratio

The dual-wavelength ratio is where the bulk of current research using AMFR's data. The DWR is the ratio of the effective reflectivity factor of the same volume at two different frequencies, generally displayed in decibels. It is shown as

$$DWR_{A-B} = dBZe_A - dBZe_B \tag{2.29}$$

where DWR_{A-B} is the dual-wavelength ratio between frequencies A and B.

For small particles, the Rayleigh scaling approximation predicts that the reflectivity factor should be largely independent of frequency. For larger particles, however, the Mie scattering regime comes into play and reduces the reflectivity factor of higher frequencies compared to those with larger wavelengths.

Equation 2.15 for dBZe was made assuming Rayleigh scattering, but that is not a necessary requirement for the forward model (converting from the physical scatterers to the received effective reflectivity factor). Given assumptions on the dielectric and drop-size distribution, the individual scatterers of a diameter can be weighted by their actual backscatter instead of the Rayleigh approximation shown in (2.14). This results in a more accurate effective reflectivity model

$$Z_e(\lambda) = \frac{\lambda^4}{\pi^5 |K|^2} \int_0^\infty N(D)\sigma(D,\lambda)dD \tag{2.30}$$

where $N(D)$ is the particle distribution at diameter D and $\sigma(D,\lambda)$ is the backscatter of particles of the assumed dielectric at diameter D and wavelength λ.

Inverting (2.30) based on a set of observations of $Z_e(\lambda)$ can provide an estimation of the drop-size distribution, as is shown in the results found in Chapter 6.

2.8.2 Differential Doppler

Doppler data from two frequencies, translated into estimates of vertical velocity, can also be used to estimate particle size distribution, particularly in nadir- and zenith-pointing radars. While doppler data is not addressed to a large extent in this work, multi-frequency doppler data from AMFR was utilized in [4] to derive drop-size distribution estimates of rain.

The theory behind multi-frequency doppler is that larger particles will drop faster than small particles. Lower frequency observations are more sensitive to larger particles, and thus will show a larger doppler velocity than the higher frequencies which are more sensitive to smaller non-precipitating particles. This can be used to quantify the drop-size distribution either through doppler moments, or through the use of raw data such as the analysis used in [4].

CHAPTER 3

SYSTEM DESCRIPTION

AMFR is a polarimetric multi-frequency radar designed for precipitation microphysics research, particularly for exploring how multiple frequencies can be used to improve upon current precipitation retrievals by helping to reduce the number of possible drop-size distributions able to give rise to the given reflectivity measurements. A table of relevant radar parameters is shown in Table 3.1.

Developed as a research instrument, AMFR was designed to avoid uncertainties in measurements that are present in many other radars. First, the system uses klystron amplifiers to generate a transmit chirp. This provides sensitivity comparable to what is available through the use of a magnetron, but avoids phase errors associated with coherent-on-receive Doppler retrieval.

Secondly, AMFR drastically reduces errors common in dual-wavelength ratio measurements by maintaining three frequencies with matched beams. The matched beams minimize parallax error and ensure that all frequencies are measuring the same volume. The use of three frequencies allows for two unique drop-size distribution measurements, and ensures that meaningful drop size distribution retrievals can be made over a wide range of particle sizes. Additionally, the presence of a lower frequency (Ku-band) allows for some resistance against the effects of attenuation by providing a less-attenuated reference for the higher frequencies.

AMFR is a mobile ground-based system. As such it is deployed on a truck-based laboratory that facilitates on-sight setup and allows the system to run independent of external power sources. The antennas and majority of radar subsections are mounted

Parameter	Ku-band	Ka-band
Frequency	13.4 GHz	35.6 GHz
Tx. Polarization	V or H	V or H
Rx. Polarization	V or H	V or H
Peak Power	5 kW	1.5 kW
Pulse Compr. Gain	19 dB	19 dB
Range Resolution	30-150 m	30-150 m
Antenna Diameter	1.8 m	0.91 m
Antenna Gain	48dB	48dB
3dB Beamwidth	0.7 deg	0.7 deg

Table 3.1: Characteristics of the 13.4 and 35.6 GHz Radars

on a two-axis positioner on the flatbed of the truck. While on the truck, AMFR enjoys approximately 270^o of azimuth scanning, with a full range of elevation angles. A picture of the mobile lab and radar is visible in Figure 3.1.

3.1 Hardware Overview

The AMFR transmit/receive subsystems were designed to be modular, able to be added or removed with minimal changes required for the rest of the system. The three frequencies share a common control field-programmable gate array (FPGA) that selects the pulse mode and pulse repetition frequency (PRF). This keeps the frequencies synchronized, and ensures that the sampling volumes are identical between the frequencies.

Each frequency has an independent FPGA and PC104 that controls transmit switch timing, the direct digital synthesizer (DDS), pulse compression, Klystron triggering, and receiver protection circuitry. The subsystems input only a common clock (10MHz), pulse triggers and a pulse-mode signal, while outputting downconverted intermediate frequency (IF) data of the same frequency, making them effectively interchangeable to the rest of the system, so long as the correct pulse compression matched filters are loaded into the data receiver computers.

Figure 3.1: Photograph of the AMFR mobile lab, positioner, and radar subsections

A common interface computer is used to control the system from inside the mobile lab. This allows access to the computers internal to the individual subsystems, and is used to display selections of data in real-time to monitor reflectivity profiles as well as system health.

The entire RF and IF systems are mounted on a two-axis positioner on the back of the mobile lab. Power and radiation controls are sent to the system via slip rings in the positioners.

3.2 RF Subsystem

The RF and IF subsystems are quite complex due to the presence of a calibration network, polarization diversity switching, pulse compression, and the high power transmitter. While there are minor differences between the Ku- and Ka-band systems, the approach and qualitative design of both frequencies is similar.

The transmit signal begins at a direct digital synthesizer (DDS), which outputs a chirp or CW signal centered at 60MHz. This signal is put through a multi-stage upconverter and inputted into the Klystron amplifier. The modulator powers the Klystron for transmit and the signal is routed at high power through the polarization switches.

Latching circulators (made by the company EMS) were chosen for the polarization network due to their low loss and ability to handle high power. As individual circulators have limited isolation, a second circulator was added in one polarization to provide additional isolation for accurate linear depolarization ratio (LDR) measurements.

The signal is then routed through a circulator out to the OMT and antenna. A small portion (-40dB) bled off in the calibration loop, and the receiver is protected by a network of three latching circulators for each polarization. Despite the attenuation and isolation of the signal during transmit, the calibration signal could cause nonlinearities in the IF receiver, so additional loss is switched into the receiver during transmit.

During the receive cycle, the receiver protection circulators open to route the signal into the receiver where it is amplified and downconverted to a 10MHz centerfrequency for sampling in the digital receiver.

The block diagram of the Ku-band system is shown in Figure 3.2, and the block diagram of the Ka-band system is shown in Figure 3.3.

3.3 Pulse Compression

AMFR uses a linear chirp pulse method of pulse compression with amplitude tapering on receive to reduce range sidelobes. This tapering achieves sidelobes better than 35dB down from the maximum while losing only a small portion of sensitivity. Tapering during both transmit and receive can achieve better results as is documented

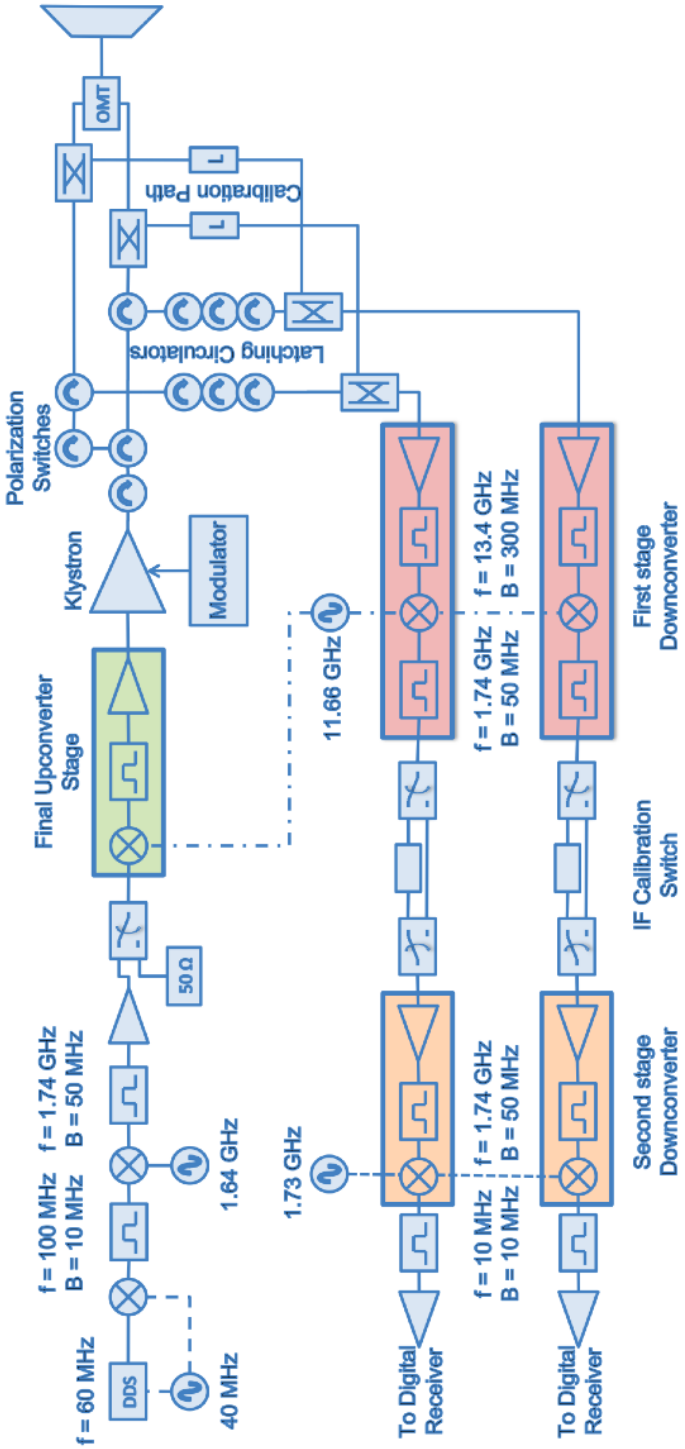

Figure 3.2: Block diagram of the Ku-band RF and IF system

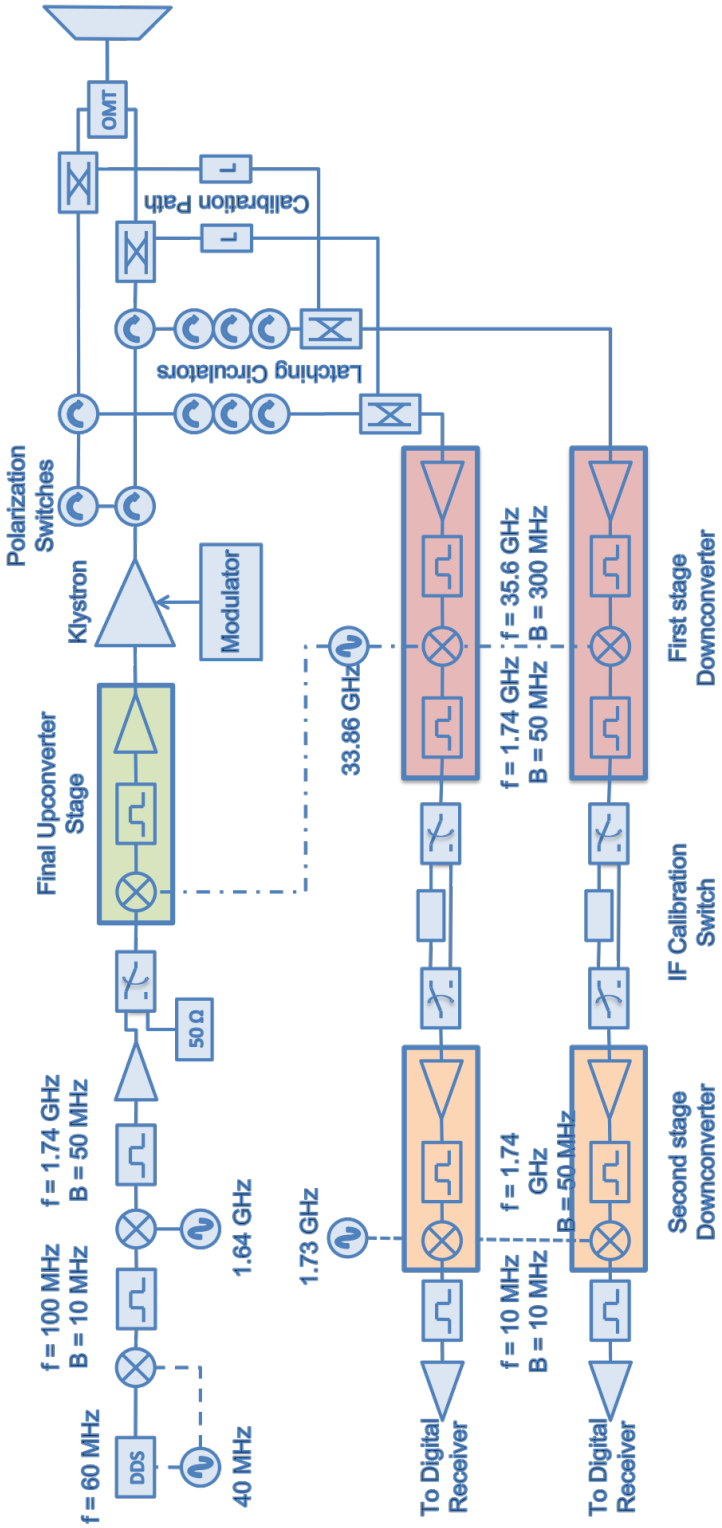

Figure 3.3: Block diagram of the Ka-band RF and IF system

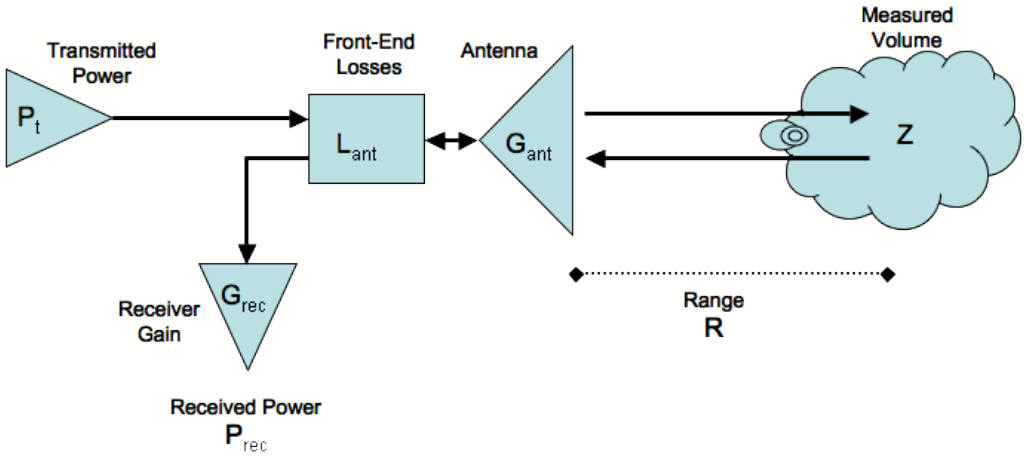

Figure 3.4: Simplified radar system used for the Radar Range Equation

in [10], however this comes with the sensitivity cost not only from the additional tapering, but also from running the klystron in the linear regime rather than in saturation. The use of non-linear chirps can be used for sidelobe suppression, however these methods suffer similarly from lost sensitivity and complexity.

As a ground-based instrument, AMFR does not have the stringent requirements for range sidelobe suppression that airborne and spaceborne instruments must adhere to. While nadir looking radars must deal with a very strong return from the ground reflection, ground-based instruments have only to deal with areas of high volume reflectivity. As such, a Hamming window was chosen for receive-only tapering, as has been documented in [4].

3.4 Reflectivity Factor Retrieval

Obtaining the Reflectivity Factor from raw radar data requires good knowledge of the internal parameters of the system. While actual systems are much more complex, they can generally be modeled for this purpose as a simplified system of a few key subsections and parameters. Figure 3.4 shows this simplified model. All of the transmitter path gains and losses up to the circulator are included in the transmitter

power P_t. All of the receiver losses and gains after the circulator are included in the receiver gain G_{rec}. The losses inclduded in both the transmitter and receiver paths (such as the waveguide to the antenna) are included in L_{ant}. The antenna gain is G_{ant}, and the range to the measurement volume under test is R. Not included in the figure is the radar's range resolution, which will be referred to as ΔR.

The Radar Range Equation is obtained using this system, and can be shown in reflectivity form as

$$P_{rec} = P_t G_{rec} \frac{G_{ant} \pi^3 \Delta R |K|^2}{L_{ant}^2 10^{18} 2^5 R^2 \lambda^2} Z. \tag{3.1}$$

The equation would naturally use the volume reflectivity, however the volume reflectivity to reflectivity factor (Z) equation (2.16) has been substituted. This version of the radar range equation uses the range resolution rather tan the pulse width due to the presence of pulse compression, where the range resolution is not limited by the pulse width. This is a reordered version of the equation as shown in [2].

The reflectivity factor is calculated by inverting (3.1) and substituting in the received power. The method AMFR used to accurately measure the rest of the parameters in the equation are detailed in Chapter 4.

3.5 Doppler Retrieval

The definition and meteorological interest of the Doppler velocity was discussed in Section 2.6. AMFR measures Doppler, like some other products, using correlation functions. The autocorrelation function of the received fields from polarization h from the same range bin at time offset $\Delta T = 1/PRF$ is shown as

$$\hat{R}_{hh}[1] = \hat{R}_{hh}(\Delta T) = \frac{1}{N} \sum_{n=0}^{N-1} E_h(t = t_n) E_h^*(t = t_n + \Delta T) \tag{3.2}$$

where the first pulse of the n'th "pulse-pair," or two pulse sequence, occurs at $t = t_n$. In this case, the horizontal polarization was arbitrarily chosen, as any co-polarization measurement would work.

The angle of this autocorrelation function at lag ΔT (discretized to an offset of one) gives an estimate of the Doppler phase defined in Equation 2.22, leading to an estimator for the mean radial velocity v,

$$\hat{v} = -\frac{\lambda}{4\pi\Delta T}\angle\hat{R}_{co}[1]. \tag{3.3}$$

With AMFR's receiver producing both in-phase and quadrature components, the final equation used to estimate mean Doppler phase is

$$\hat{v} = -\frac{\lambda}{4\pi\Delta T}\angle\left(\frac{1}{N}\sum_{i=0}^{N=1} I_i I_{i+\Delta T} + Q_i Q_{i+\Delta T} - j\left(I_i Q_{i+\Delta T} - Q_i I_{i+\Delta T}\right)\right) \tag{3.4}$$

where i corresponds to the first return from the i^{th} pulse-pair and $i+\Delta T$ corresponds to the consecutive return of the same polarization.

3.6 Differential Phase Retrieval

The polarization scheme for AMFR utilizes alternating vertical and horizontal pulses while receiving both polarizations, or what is known as a polarization diversity radar. The basics of radar polarization types is discussed in Section 2.7.1.

Because only one polarization is transmitted at a time, differential reflectivity and linear-depolarization ratio can be measured through (2.25) and (2.26). More difficult to measure is the specific differential phase. Simultaneous-transmit radars can directly measure this by directly comparing the phase of receive at both polarizations, however as the product is defined at zero time-lag, this can not be done with polarization diversity radars.

The equation for differential phase shown in Section 2.7.3 can be modified slightly to show that it is defined for zero time lag, as

$$\Phi_{dp}(r)(t) = \angle T_h(r)(t) - \angle T_v(r)(t). \tag{3.5}$$

The differences in phase measured by AMFR though a consecutive horizontal then vertical pulse would include a time-lag equal to the PRF time, called ΔT for this case. If we call the difference in phase between the consecutive pulses $\Phi_{\Delta T}$ then the difference in phase measurable by a polarization diversity radar can be given as

$$\Phi_{\Delta T}(r)(t) = \angle T_h(r)(t) - \angle T_v(r)(t + \Delta T). \tag{3.6}$$

There are three physical operations at play in creating this value $\Phi_{\Delta T}$ as was shown in [9]. The first, but not the dominant, is the difference in propagation speed between the horizontal and vertical channels; this information is embodied in the differential phase, Φ_{dp}. The second and most dominant is the Doppler effect (discussed in Section 2.6), the phase associated with the radial movement of reflectors in the integration volume between the pulse times. Third, there is decorrelation of the two phases due to random movement of reflectors in the volume and propagation paths.

The decorrelation effects are unavoidable, but expected to be small with pulse repetition frequencies (PRF) on the order of several kilohertz. The effects of radial movement can be removed through subtracting the Doppler phase $\Delta\Phi$ as defined in (2.22), as

$$\Phi_{dp} \approx \Phi_{\Delta T} - \Delta\Phi. \tag{3.7}$$

While [9] demonstrated the method for Φ_{dp} retrieval from a strictly alternating polarization diversity radar, AMFR uses alternating two-pulse sets to allow for a good estimate of Φ_{dp}, and thus KDP while maintaining doppler measurements unen-

cumbered by differential phase effects.. A small subsample of pulses could be shown as

$$...V|_{t=t_o-\Delta T},\, H|_{t=t_o},\, H|_{t=t_o+\Delta T},\, V|_{t=t_o+2\Delta T},\, V|_{t=t_o+3\Delta T},\, H|_{t=t_o+4\Delta T}... \tag{3.8}$$

where H and V are the horizontal and vertical pulses and ΔT is $1/PRF$. It is convenient to discretize this series into

$$...V[-1],\, H[0],\, H[1],\, V[2],\, V[3],\, H[4]... \tag{3.9}$$

where pulse $H[n]$ occurs at time $t = t_o + n\Delta T$.

This polarization scheme produces four types of constant-range autocorrelation estimates at time offset ΔT (1/PRF):

$$\hat{R}_{hh}[1] = \frac{1}{M}\sum_{i=0}^{M-1} H_{4i}^{*} H_{4i+1}, \tag{3.10}$$

$$\hat{R}_{hv}[1] = \frac{1}{M}\sum_{i=0}^{M-1} H_{4i+1}^{*} V_{4i+2}, \tag{3.11}$$

$$\hat{R}_{vv}[1] = \frac{1}{M}\sum_{i=0}^{M-1} V_{4i+2}^{*} V_{4i+3}, \tag{3.12}$$

and

$$\hat{R}_{vh}[1] = \frac{1}{M}\sum_{i=0}^{M-1} V_{4i+3}^{*} H_{4i+4}. \tag{3.13}$$

Equations 3.10 and 3.12 are not used for the differential phase measurement, and are reserved for doppler retrievals per (3.3).

As is derived in [9], the angles of (3.11) and (3.13) can be shown as:

$$\angle R_{hv}[1] = \Re\left(k_{\text{eff}}^{h} - k_{\text{eff}}^{v}\right) - \frac{4\pi\Delta T}{\lambda} v = \Phi_{dp} + \Delta\phi_{doppler} \tag{3.14}$$

and

$$\angle R_{vh}[1] = \Re\left(k_{\text{eff}}^{v} - k_{\text{eff}}^{h}\right) - \frac{4\pi\Delta T}{\lambda} v = -\Phi_{dp} + \Delta\phi_{doppler} \tag{3.15}$$

where k_{eff}^h and k_{eff}^v are parts of the transmission matrix shown in (2.6), ΔT is the time between pulses (1/PRF), λ is the wavelength, and v is the mean radial particle velocity. Equations 2.28 and 2.23 were substituted in to produce a more clear picture.

It is clear from the result shown in (3.14) and (3.15), an estimator for the differential phase can be made by finding the difference between $\hat{R}_{hv}$ and $\hat{R}_{vh}$, such as

$$\hat{\Phi}_{dp} = \frac{1}{2}\left(\angle\hat{R}_{hv}[1] - \angle\hat{R}_{vh}[1]\right). \tag{3.16}$$

While this Φ_{dp} retrieval was not available during the 2007 C3VP field campaign, subsequent changes to the pulse scheme and data acquisition system now allow for differential phase measurements.

3.7 Real-Time Processing

It is impractical to produce the radar products listed above in real time during data collection. Some calculations such as the angle of complex numbers are computationally intensive and are best left for post-processing. Other processes such as converting the power at the analog-digital converter to an estimate of reflectivity requires careful calibration, as will be discussed in Chapter 4.

On the other extreme, recording all received data is also impractical. Each frequency has two channels sampling 1024 range bins at 2800 pulses per second. With each channel having 16 bits each of I and Q, the result is 183Mbits/sec. The raw data provides for some interesting processing, as was shown in Ninoslav Majurec's work of AMFR differential doppler spectrum analysis [4], but one hour of three-frequency data would result in more than 250GB of data. This makes continuous raw data collection difficult to work with.

As such, AMFR's digital receiver generally records the autocorrelation function data, allowing for specific data products to be completed in post-processing while removing the bulk associated with raw data retrievals.

Referring to the sequence of polarization diverse pulses shown in (3.9), for each polarization, the autocorrelation function at time offset zero is proportional to the power in the radar receiver. This is used for power measurements such as $dBZe$, Z_{dr}, and LDR. As such, the autocorrelations

$$\hat{R}_{co,h}[0] = I_h^2 + Q_h^2 \tag{3.17}$$

and

$$\hat{R}_{cr,h}[0] = I_v^2 + Q_v^2 \tag{3.18}$$

provide the power measurements for both the co-pol (transmit h, receive h) and cross-pol (transmit h, receive v) power products. These results are averaged over a period of time, typically 200-400 pulses per polarization.

The doppler and differential phase measurements both come from autocorrelations at time offset ΔT. Pulse pairs of the same polarization are used for Doppler while pulse pairs of switching polarization are used for differential phase. Unlike the autocorrelation at time zero, these values remain complex, shown as

$$\hat{R}[1] = I_i I_{i+1} + Q_i Q_{i+1} + j\left(I_i Q_{i+1} - I_{i+1} Q_i\right). \tag{3.19}$$

These results are also averaged (per polarization set $R_{hh}[1]$, $R_{hv}[1]$, $R_{vv}[1]$, and $R_{vh}[1]$) and used to produce doppler and differential phase measurements in post-processing.

CHAPTER 4

CALIBRATION

The approach of the calibration of AMFR is to use measured internal parameters to monitor gain variations and provide useable scientific moments from the radar data. The system uses an internal calibration path that can monitor gain changes in the active RF components. This approach was instrumental in correcting for hardware failures that occurred due to the extreme weather conditions during the C3VP experiment during January 2007. The calibration approach and results following the C3VP experiment were first documented in [6].

4.1 Calibration Methodology

The Ku- and Ka- band channels of AMFR feature attenuated calibration paths coupled from the transmitter to the receiver, as can be seen in Figure 4.1. This allows constant monitoring of the active components, particularly the output power of the Klystron amplifier.

To protect the receiver during transmit, as well as to allow the coupled calibration signal to be distinguished from leaked transmit power, circulators are used to channel power out the antenna and isolate the receiver from the high power signal.

AMFRs calibration is taken directly form the calibration path data. It begins with the radar range equation equivalent to what is shown in [2] for the received signal as a function of internal radar parameters, reflectivity (in units of mm^3/m^3), and range shown as

$$S_{rec} = P_t G_{rec} \frac{G_{ant} \pi^3 \Delta R |K|^2}{L_{ant}^2 10^{18} 2^5 R^2 \lambda^2} Z. \tag{4.1}$$

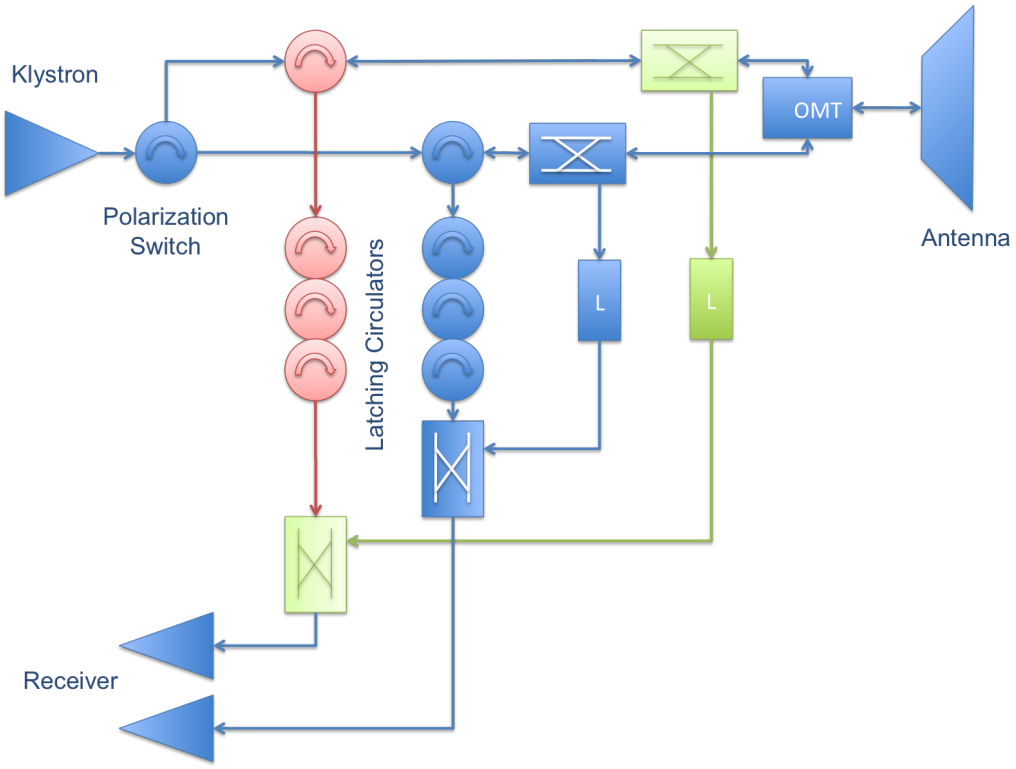

Figure 4.1: Calibration network showing calibration signal path (green) and the leakage signal path (red)

In (4.1), S_{rec} is the received signal power with arbitrary scaling, defined as

$$S_{rec} = \sum_{i=0}^{M-1} \hat{R}_{co}[0]. \tag{4.2}$$

P_t is the peak transmit power modified by the pulse compression gain, G_{rec} is the receiver gain, G_{ant} is the antenna gain, L_{ant} is the front-end loss not included in the internal calibration loop, R is the range, and ΔR is the range resolution. The received signal during the calibration is simpler, only being effected by system gains and losses, and can be written as

$$S_{cal} = \frac{P_t G_{rec}}{L_{cal}} \tag{4.3}$$

where S_{cal} is the calibration signal received during transmit, and L_{cal} is the measured loss of the calibration path. Equation 4.3 is used to provide an estimator of the product of the transmit power and receiver gain

$$\widehat{P_t G_{rec}} = S_{cal} L_{cal}. \tag{4.4}$$

By substituting $\widehat{P_t G_{rec}}$ from the calibration data back into the radar range equation and solving for reflectivity, the calibrated reflectivity signal is made independent of the transmitted power and gain of the receiver [12].

$$\hat{Z} = \frac{S_{rec}}{\widehat{P_t G_{rec}}} \frac{L_{ant}^2 2^5 R^2 \theta^2 10^{18}}{G_{ant} \pi^3 \Delta R |K|^2}. \tag{4.5}$$

This remains true so long as the gain is stable throughout whatever period of time the calibration signal has been averaged.

4.2 Calibration Path Data

The choice of how to best implement this calibration approach was driven by the shape and stability of the internal calibration loop data. During the C3VP experiment, two sets of 200 compressed 10μs pulses were used along with one set of 200 uncompressed 1μs pulses. This provided good SNR for the extended range of the radar while ensuring that the first two kilometers were also covered.

As can be seen in Figure 4.2, the 1μs calibration signal suffers from heightened instability caused by the delay in the latching of the receiver isolation circuit. Additionally, during periods of intense precipitation near the radar, it becomes unclear when the calibration path data ends and the reflectivity data begins. Due to these concerns, the pulse compressed data was used for internal calibration, and another approach was used for the 1μs pulse, as will be described in Section 4.3.

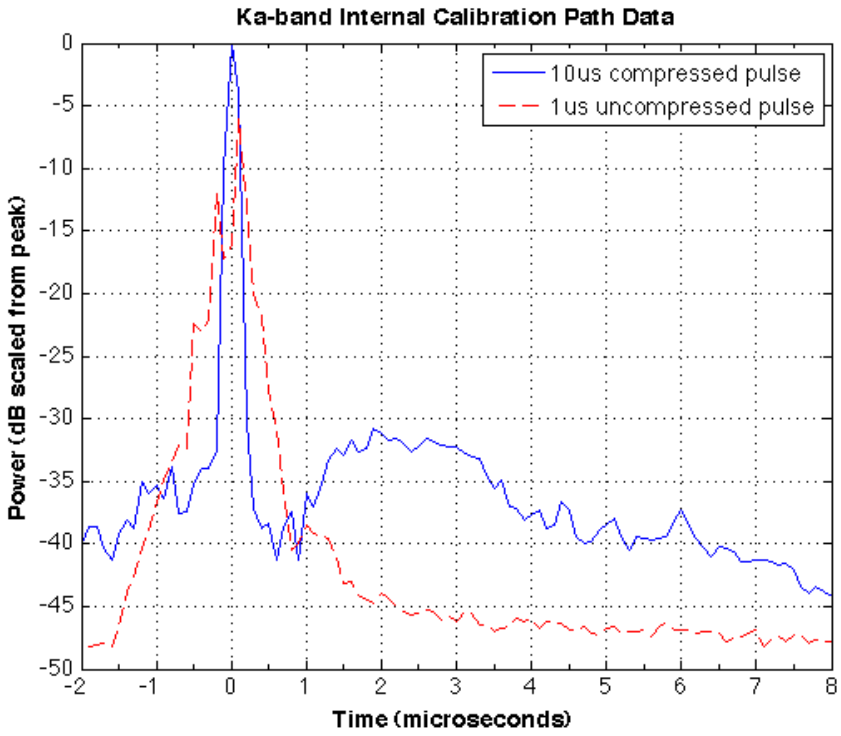

Figure 4.2: Internal Calibration Signals (10μs and 1μs)

The 10μs pulses were ideal for internal calibration. As can be seen in Figure 4.2 the long pulse and compression cause a clear spike during transmit with very low power afterward. The signal adjacent to the transmit spike is a combination of pulse compression side-lobes, artifacts from the receiver switching, and some signal resulting from side-lobes associated with precipitation targets. Despite these sources, the range bins adjacent to the transmit pulse are more than 30dB down.

To ensure that jitter between the transmitter and the IF receiver does not move the calibration pulse out of the expected range bins, the bins just outside the main pulse were also summed when estimating the transmit power. This minimized the effects caused by timing jitter, and resulted in the most stable calibration. The added power does not negatively effect the calibration as these range bins are very small compared to the peak.

4.3 Combining the Pulse Lengths

The primary calibration was done with the 10μs compressed pulse due to its high signal-to-noise ratio (SNR) and the absence of adjacent reflectivity data in the return. It was determined that the 1μs data would best be calibrated by transferring the 10μs calibration through matching volume reflectivity. This approach has the advantage of providing consistently calibrated images while avoiding the problems with the 1μs calibration loop detailed in Section 4.2. The disadvantage is that it requires reflectivity of a reasonable SNR just outside of the 10μs blind region and reduces the stability of the 1μs calibration if the transmit power estimator is averaged over too short a region.

As can be seen in Figure 4.3, the stitched reflectivity image shows good agreement between the 10μs and 1μs sections, implying a successful calibration of the 1μs pulse. The image is a time-series that includes a planned position indicator (PPI; which is just an azimuth scan at a fixed elevation angle) scan as well as five range height indicator (RHI; this is an elevation scan at a fixed azimuth angle) scans from through nine minutes into the plot. The Ku-band shows a second cloud layer in the RHI's. This clearly shows the increased sensitivity of the pulse-compressed data, as the second cloud layer is not visible in the 1μs data.

4.4 Calibration Uncertainty

There are three types of errors associated with this calibration method. The first is calibration biases (in decibels) caused by imperfect knowledge of calibration loop losses and components outside the loop. These biases are long-term errors found in radar data, however because they are stable, data sets can be accurately compared over long periods of time even with these biases.

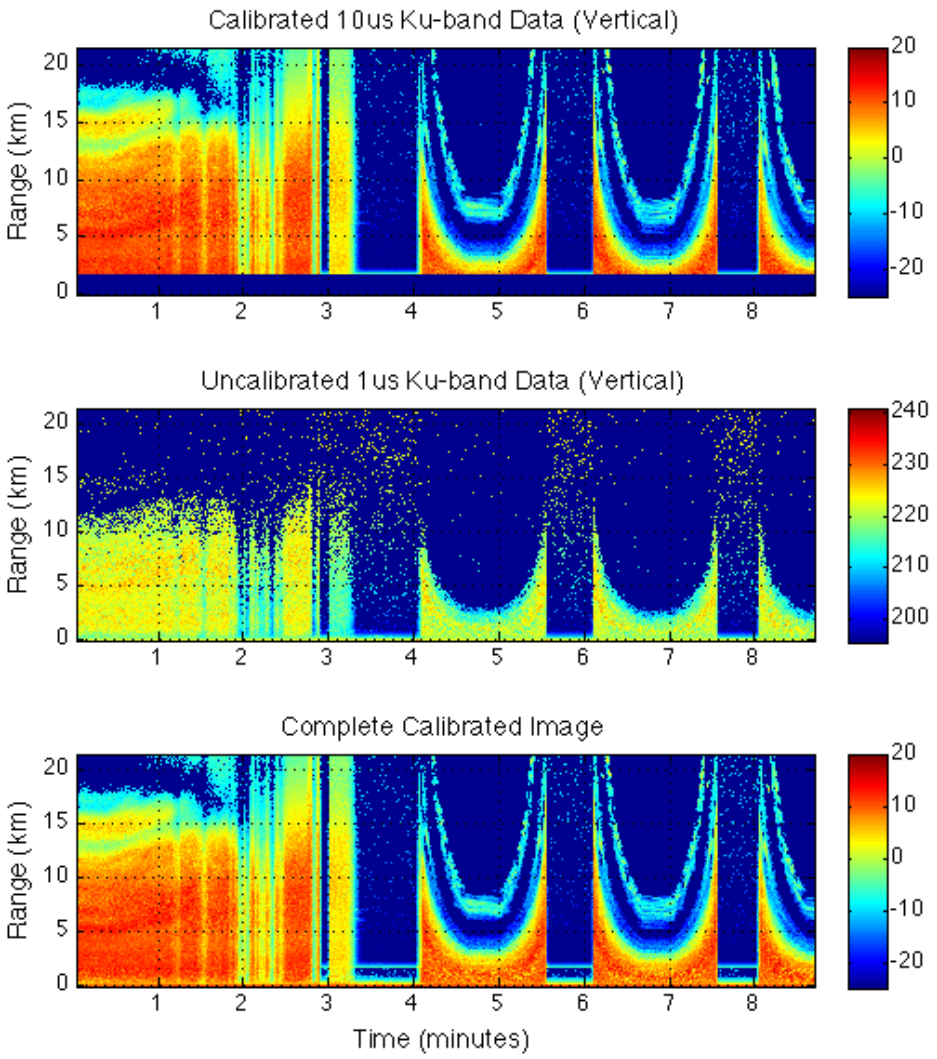

Figure 4.3: The calibrated 10μus data, uncalibrated 1μs data, and combined image. The data is from the vertical polarization channel, and shows a PPI scan followed by 5 RHI scans.

4.4.1 Calibration Biases

It should be noted that calibration biases most strongly effect the Dual-Wavelength Ratio retrievals, as the signature tends to be smaller than the reflectivity retrieval and the biases of both frequencies come into play.

For AMFR, these biases were minimized by making careful S-parameter measurements of calibration loop and front-end losses. The vendors provided data on the antennas, however making precise beam measurements is difficult, and has not been performed since UMass has received the antennas. A solar calibration, or using the sun to map the antenna beam as well as calibrate the receiver is possible, however it was not performed due to difficulties in making accurate measurements at low signal to noise ratios.

One source of bias in an internal calibration scheme is the interaction of the known calibration signal with the undesired leakage signal. The loss in the calibration path (L_{cal}) consists of the two couplers combined with the added attenuation in the calibration path. The loss of the leakage signal (L_{leak}) experiences is the combined directivity of the fixed coupler (or the return loss of the antenna) and the latching receiver-protection circuits.

As the leakage signal and the calibration signal are correlated, they can not be simply combined or subtracted. Additionally, the phase between them is very difficult to measure due to the extreme levels of attenuation involved. Because of this, it is necessary to use voltage rather than power to determine possible errors. The combined received calibration signal S_{cal} (in power) received during transmit can be shown as

$$S_{cal} = \left(V_t \left(\frac{1}{\sqrt{L_{cal}}} + \frac{1}{\sqrt{L_{leak}}} \cos\left(\Delta\phi\right) \right) \right)^2 \frac{1}{Z_o} \tag{4.6}$$

where V_t is the transmitted voltage, Z_o is the characteristic impedance of the system, and $\Delta\phi$ is the difference in phase between the two signal paths. The error due to this

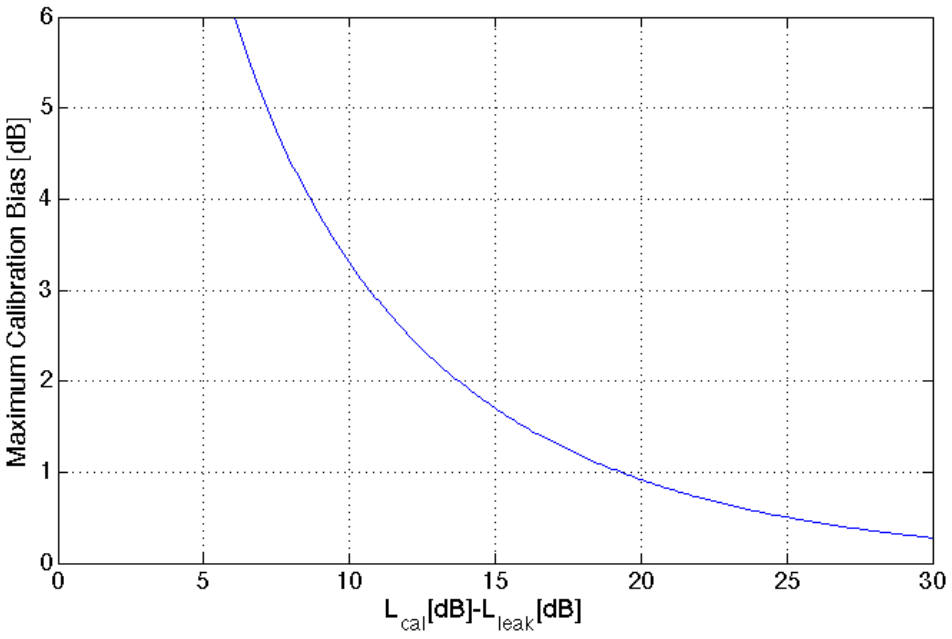

Figure 4.4: Possible calibration bias as a function of the difference in loss between the calibration signal and the transmitter leakage signal

leakage signal can be shown in decibels as the ratio of Equation 4.6 with the ideal case of infinite leakage loss. The resulting equation for error ΔCal is

$$\Delta Cal = 10log_{10}\left(\left(1+\frac{\sqrt{L_{leak}}}{\sqrt{L_{cal}}}\cos\left(\Delta\phi\right)\right)^2\right). \tag{4.7}$$

The error will thus be maximized when the two signal line up directly in- or out-of-phase. The maximum possible error due to this interaction as a function of of the ratio of signal loss to calibration path loss (in dB) is shown in Figure 4.4. The isolation of AMFR's receiver protection electronics provide for better than one decibel accuracy in the calibration estimators for existing data sets. A calibration path modification has since improved this performance, as is detailed below.

In radar design, isolation in the receiver path during transmit is expensive due to the need for low loss, high isolation, and rapid switching. For AMFR, the decision was made to use a network of latching circulators in each of the receiver paths. These

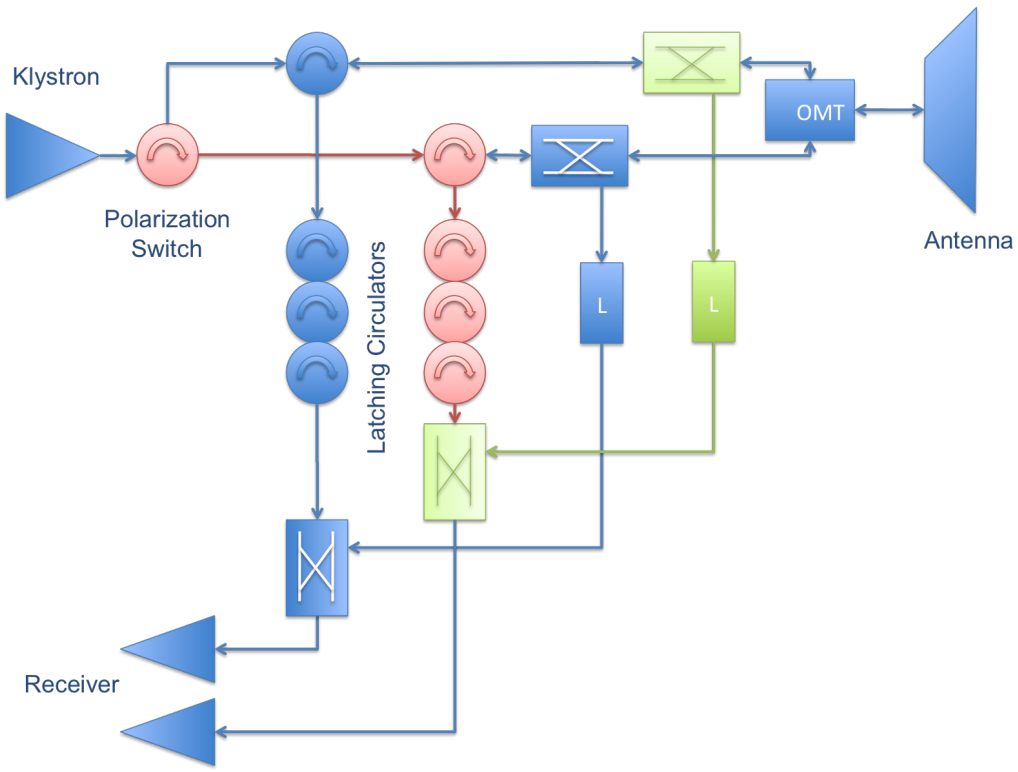

Figure 4.5: Modified calibration path hardware designed to reduce calibration uncertainty due to leaked power. This figure shows the calibration signal path (green) and the leakage signal path (red). This diagram can be contrasted with the original design shown in Figure 4.1

components have and advantage in being very low loss with ample switching speed. The disadvantage lies in the limited isolation in each component.

The possible bias in AMFR's calibration path was reduced after C3VP by feeding the signal coupled out of each polarization's transmitter path into the path of the other polarization, as is demonstrated in Figure 4.5. This method assumes that receiver gain and transmitter power remains constant over the span of several pulses. This is a reasonable approximation as AMFR's calibration was not done pulse-to-pulse.

The advantage to this modification is the polarization switch contributes to the isolation in the receiver path during transmit. This can moderately decrease biasses due to the leaked signal interacting in- and out-of phase with the calibration signal.

The major disadvantages are that pulse-to-pulse calibration is impossible, and in that problems in one polarization network, such as a damaged circulator, may result in bad calibration for both channels. It was determined that this risk is acceptable for the increased performance. An alternative solution to decrease possible bias would be to add additional latching circulators to each channel, however the cost associated with such a change would be considerable.

The possible error biases from transmitter leakage have not been quantified due to the extreme levels of isolation, however the new calibration paths have reduced this source of bias to levels below that caused by antenna pattern and component loss measurements.

4.4.2 Calibration Stability

Calibration stability is more important than calibration accuracy, and is the driving factor in the AMFR calibration approach. While both sources of error can corrupt individual measurements, drifts in calibration make it more difficult or impossible to accurately compare multiple data sets.

System drifts are caused by changes in temperature and aging. In this respect passive components tend to be very stable. Ferrite components perform worse, with active components such as amplifiers having the most variation in amplitude as a function of temperature and component age. Historically, high power amplifiers and microwave sources are a particular problem.

The primary goal behind the internal calibration was to minimize the drifts in the data. Originally, it was planned that the MIRSL thermal chamber would be used to track calibration path losses with with temperature, however this was skipped in favor of more pressing hardware and data analysis work.

CHAPTER 5

THE CANADIAN CLOUDSAT/CALIPSO VALIDATION PROJECT

AMFR participated Canadian CloudSat/CALIPSO Validation Project (C3VP) located in south central Ontario during January 2007. The experiment involved a wide collection of ground based instruments as well as airborne instrumentation during CloudSat fly-overs.

Despite difficulty with hardware due to the extreme environments experienced during the experiment, AMFR produced good results at Ku- and Ka-band, with reflectivity factor, doppler, dual-doppler, linear depolarization ratio, and dual-wavelength ratio retrievals, as well as raw data. Due to the polarization scheme utilized at the time, differential phase measurements were not possible.

The data most of interest from AMFR was taken during a wide-spread winter storm event during January 21-22, 2007. The storm featured dual cloud-layers with large aggregate snowfall, as is documented in the science logs from the experiment [8]. AMFR was able to take data throughout this winter event, and the multi-frequency data shows information about the the precipitation size during different parts of the storm.

5.1 Environmental and Hardware Difficulties

The coldest temperature recorded in the AMFR mobile lab during the experiment was -27° C, which proved punishing to the radar hardware. Despite attempts to keep the instrument warm through active heating as well as insulation, it was designed to

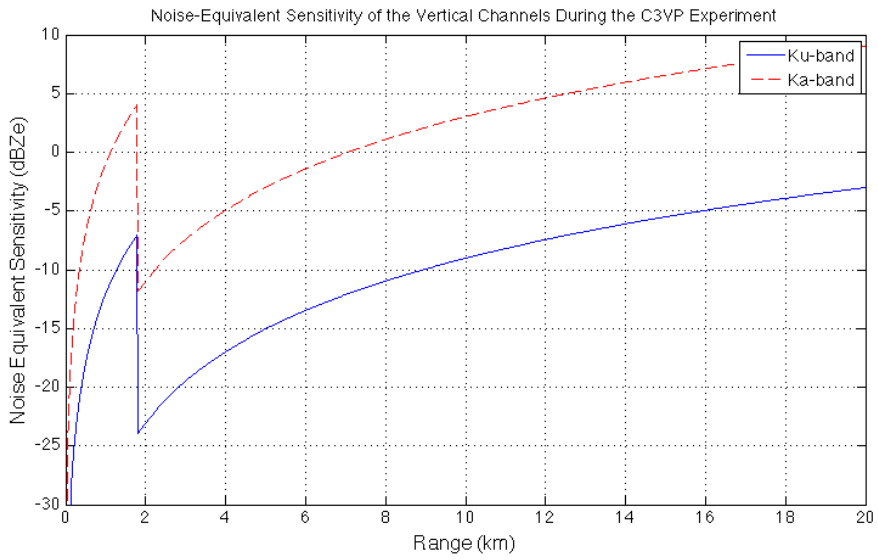

Figure 5.1: The noise-equivalent sensitivity of the Ku- and Ka-band vertical channels during the C3VP experiment. Note the reduced sensitivity experienced by the Ka-band channel, likely due to the extreme cold experienced during the experiment.

dissipate heat so as to not overheat during normal operating conditions, and the system components were consistently below design operating temperatures.

The Ka-band in particular sustained damage from the cold temperature. It is expected that poor reaction from the high-power latching circulators in those conditions caused one of the LNA's to experience an overpowered spike during transmit that caused the horizontal receiver to be inoperable during the experiment. Additionally the Ka-band radar experienced a consistent 19dB power loss during C3VP which has not been replicated since.

Despite the extreme power loss, the internal calibration allowed for a good calibration and dual-wavelength ratio (DWR) retrievals, albeit at a reduced sensitivity. The noise-equivalent sensitivity of the AMFR system (vertical channels) during the experiment is shown in Figure 5.1.

5.2 Cross-calibration with the King City Radar

During the C3VP, several RHI (i.e. fixed azimuth changing elevation) scans were made concurrently (within several minutes) between the AMFR radar and the Environment Canada King City weather radar along the same azimuth angle. The King City radar is a polarimetric C-band instrument with a range resolution of 125 meters for the concurrent RHI scan (as opposed to AMFR's 30m resolution). While range and beamwidth differences resulted in a larger observation volume for the King City radar, the comparison still provides valuable information about the quality of the AMFR calibration.

The reflectivity comparison was done during a widespread winter storm with light to moderate snowfall [8]. Due to possible attenuation at the longer ranges at the higher frequencies of AMFR and ground clutter at lower elevations and shorter ranges, a section of reflectivity data 2km to 4km in height and 4km to 8km in horizontal range from AMFR was compared. The AMFR and King City radar vertical reflectivity images are shown in Figure 5.2.

Note that the comparison between King City and the Ka-band system is not particularly useful due to the presence of Mie scattering in the Ka-band data. However, AMFR's average calibrated Ku-band reflectivity was found to match the average King City reflectivity to within 1.5dB for both polarizations. This is within the uncertainty expected in the comparison.

5.3 Radar Products and Observations from 22 January 2007

The 22 January 2007 synoptic winter storm event is the most important test case from the C3VP experiment. It was a large storm and was measured by a large array of ancillary ground instrumentation.

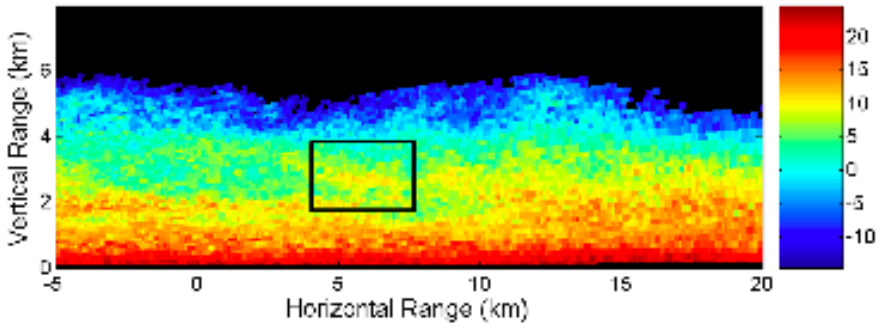

(a) King City Radar

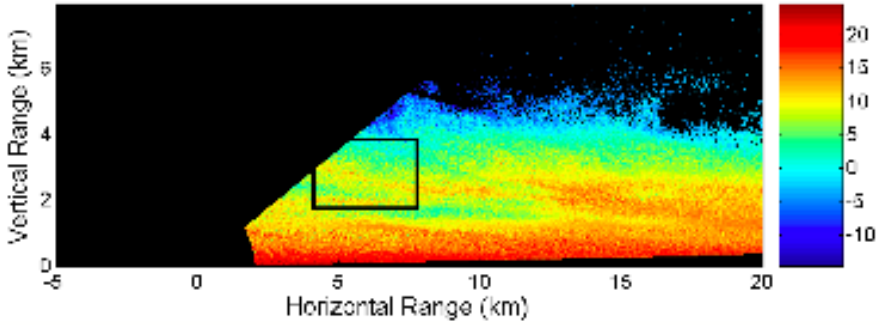

(b) AMFR Ku-band

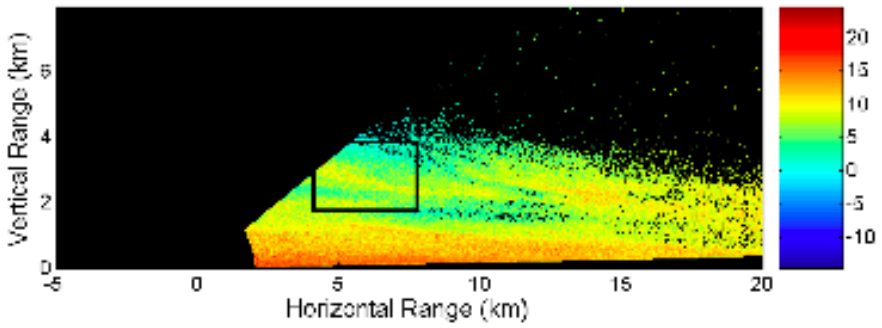

(c) AMFR Ka-band

Figure 5.2: Comparison of the King City Radar and AMFR calibrations (dBZe). The compared volume is highlighted by a black box

5.3.1 3:30 to 4:30 UTC

This period featured a vertically stratified two-layer storm. AMFR showed dual-wavelength ratios as high as 15dB for the lower layer, an indication of large aggregate snowfall, as attenuation is not a large issue for either frequency with cold dry snow.

The second cloud layer, from 4 to 5.5km in vertical elevation showed a low dual-wavelength ratio around zero dB. This shows the presence of small ice crystals, as would be expected from a high-altitude non-aggregate layer. Dual-wavelength data of this layer was not always available due to the reduced sensitivity of the Ka-band radar during this experiment.

Towards the end of this period, reflectivies and the dual-wavelength ratio weaken, as the layers begin to merge.

5.3.2 4:30 to 5:30 UTC

During this period, the two cloud layers are seen to merge, and the area around the radar experienced a temporary lull in heavy precipitation. This corresponded with decreased reflectivity and Dual Wavelength Ratio in the area of the radar, although for most of this period heavy precipitation was visible in data from several kilometers away. Scans were directed towards the areas of heaviest precipitation.

Towards the end of this time period, an area of heavy reflectivity and large dual-wavelength ratio moved into the scanning area and approached the radar location.

5.3.3 5:30 to 6:30 UTC

Heavy precipitation blanketed the area for some time before weakening in both reflectivity and dual-wavelength ratio. Reflectivities during this time reached the maximum recorded by AMFR during this storm, and the weaker dual-wavelength ratio suggests that the previously large flakes have been replaced by smaller ice particles.

CHAPTER 6

QUANTITATIVE SNOW-SIZE DISTRIBUTION RETRIEVAL AND COMPARISON WITH GROUND TRUTH

The C3VP experiment provided an excellent opportunity to develop and evaluate scientific models by using the wide array of instrumentation available. The data produced by AMFR during the high-priority date of 22 January 2007 was mapped to the results of a model provided by Bob Meneghini and Liang Liao at the NASA/Goddard Space Flight Center, and compared with the ground truth provided by the Snowflake Video Imager (SVI) developed by NASA/Goddard Space Flight Center and the University of North Dakota [7].

6.1 Meneghini / Liang Dual Wavelength Ratio Model

The model used to transform the dual-wavelength ratio data produced by AMFR into an estimate of drop-size distribution was developed by Bob Meneghini and Liang Liao at the NASA/Goddard Space Flight Center. It is a thorough model based on the scattering properties of distributed reflectors based on flexible input parameters. The output of the model includes the dual-wavelength ratio for a range of median mass diameters which is used as a lookup table for AMFR's DWR data. Details of the model, including snow-size and particle density retrievals are shown in [3].

The implementation of the model as used here is shown in Appendix B, and uses a Gamma distribution

$$N_\Gamma(D) = N_0 D^\mu exp\left(\frac{-(3.67+\mu)D}{D_0}\right) \tag{6.1}$$

where $N_\Gamma(D)$ is the distribution in units of $mm^{-1}m^{-3}$. The total volume reflectivity for each median mass diameter (D_0) is given by the sum of the backscatters according to the Mie solution weighted by their distribution This can be approximated with an integral

$$Z_e(\lambda, D_0) = \frac{\lambda^4}{\pi^5 |K|^2} \int_0^\infty N(D, D_0)\sigma(D, \lambda)dD \tag{6.2}$$

to produce an estimate of the effective reflectivity factor for a given distribution and wavelength. This result is also shown in Section 2.8.1.

The Mie scattering calculations require the dielectric constant of the precipitation. For rain, the dielectric constant of water is well known. Snow is a composite of ice, air, and sometimes water. This makes for a wide range of possible dielectric constants. The extreme cold during the C3VP experiment simplifies the calculations by ensuring that the snow was dry. As such, the model

$$\frac{\epsilon'_s - 1}{3\epsilon' s} = \frac{\rho_i}{\rho_s}\left(\frac{\epsilon'_i - 1}{\epsilon'_i + 2\epsilon'_s}\right) \tag{6.3}$$

found in [11] is used to determine the dielectric constant of dry snow as a function of snow density. In (6.3), ϵ'_i is the relative dielectric constant of ice, ϵ'_s is the dielectric constant of snow, ρ_i is the density of ice, and ρ_s is the density of the snow.

The output of the model for parameters typical of a winter storm are shown in Figure 6.1. It shows the DWR for rain and several densities of snow as a function of the median mass diameter of a Gamma distribution with $\mu = 0$. The results show that the DWR is largely independent of snow density for distribution with D_0 less than 4 mm. It also shows that rain will have a slightly negative DWR for small particles.

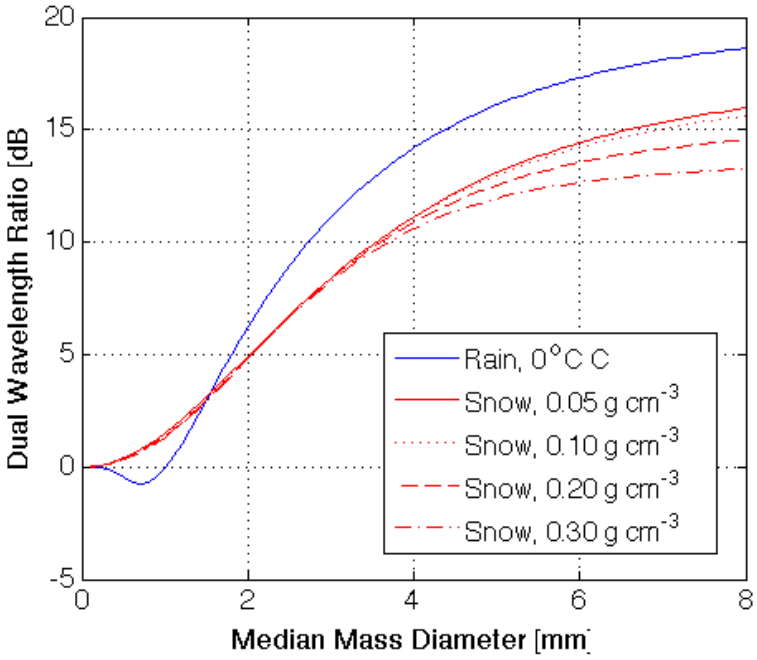

Figure 6.1: The output of the NASA DWR/D_0 model used in this analysis

6.2 AMFR Dual-Wavelength Ratio Data

The model described in Section 6.1 is a forward model (going from the physical processes to the received dual-wavelength ratio), a lookup table of results is used for the reverse model (going from the received dual-wavelength ratio to an estimate of the physical processes). Figure 6.2 shows one example of an RHI taken at 6:14 on 22 January 2007 during the C3VP experiment. The snow-density used is 0.05 g/m^3 due to the large aggregate nature of the snowfall.

As can be expected, the higher reflectivities found under two kilometers vertical distance correlate strongly with a higher dual-wavelength ratio, and thus a higher median-mass diameter. A scatter plot of the measured dual-wavelength ratio vs. reflectivity is shown in Figure 6.3. The points on the plot are evenly spaced individual pixels from different vertical distances from the data shown in Figure 6.2. This plot clearly shows both the correlation of reflectivity and dual-wavelength ratio. Addition-

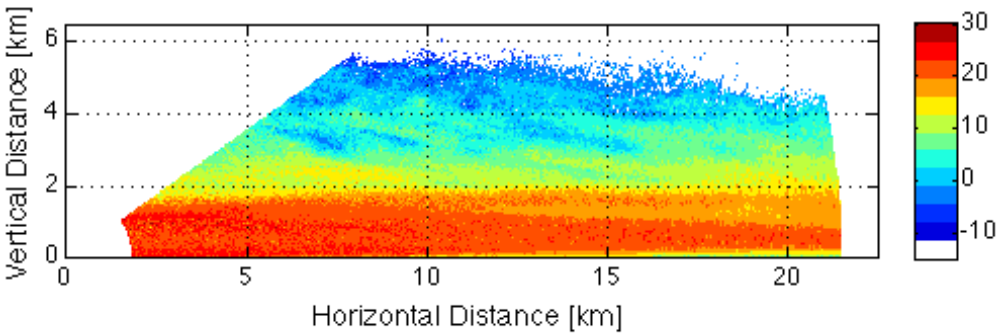

(a) Ku-band Reflectivity (dBZe)

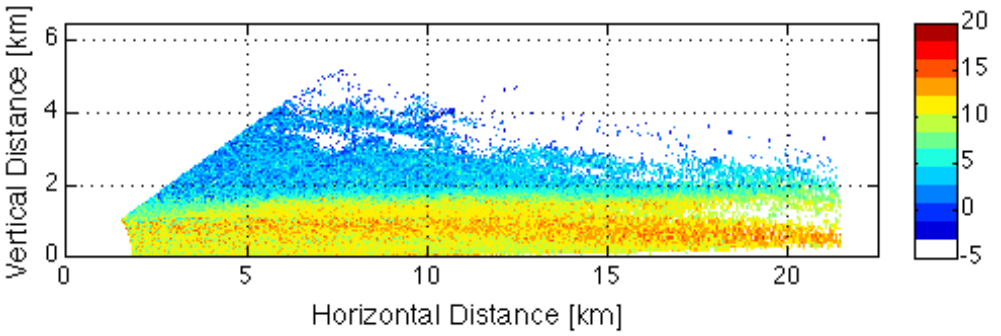

(b) Dual-Wavelength Ratio (dB)

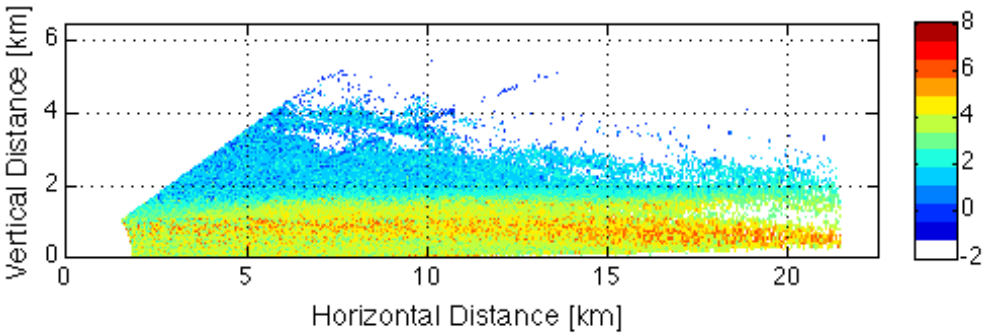

(c) Median-Mass Diameter (mm)

Figure 6.2: A median-mass diameter retrieval taken by AMFR at 6:14 on 22 January 2007

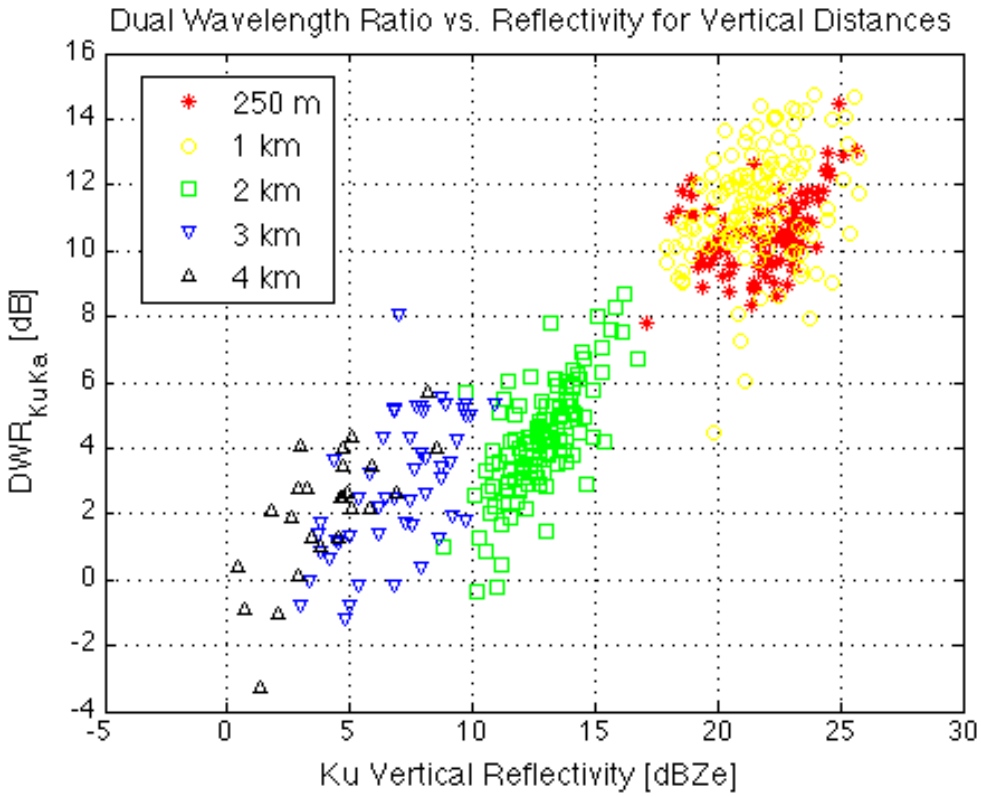

Figure 6.3: A scatter plot of the dual-wavelength ratio vs. Ku-band reflectivity of individual pixels from Figure 6.2. The colors correspond to different vertical distances from the radar.

ally, it shows that the particles near the ground were generally both more reflective and larger than those higher in the cloud structure.

A subset of the data shown in Figure 6.2 provides a more clear picture of median-mass diameter changes with vertical elevation. The average d_o from a slice of the RHI shown in Figure 6.2 at 7km horizontal distance is shown in Figure 6.4.

6.3 Snowflake Video Imager (SVI)

The Snowflake Video Imager (SVI) is an optical ground-based instrument developed by NASA/GSFC and the University of North Dakota [7]. The instrument provides minute-spaced retrievals of drop-size distribution, measured as a snow-size

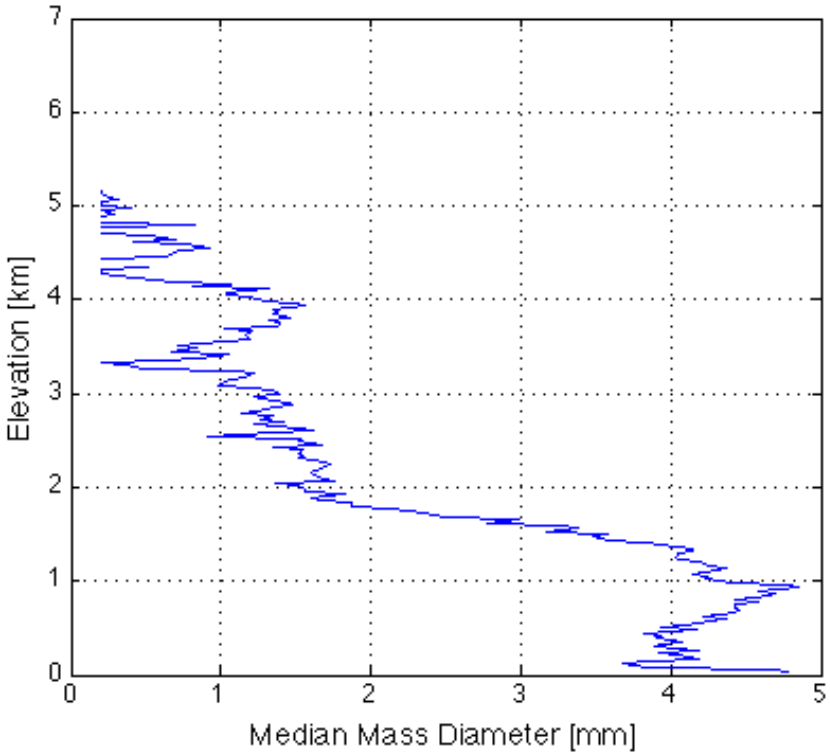

Figure 6.4: A profile of median-mass diameter vs. elevation taken from a slice of data from Figure 6.2

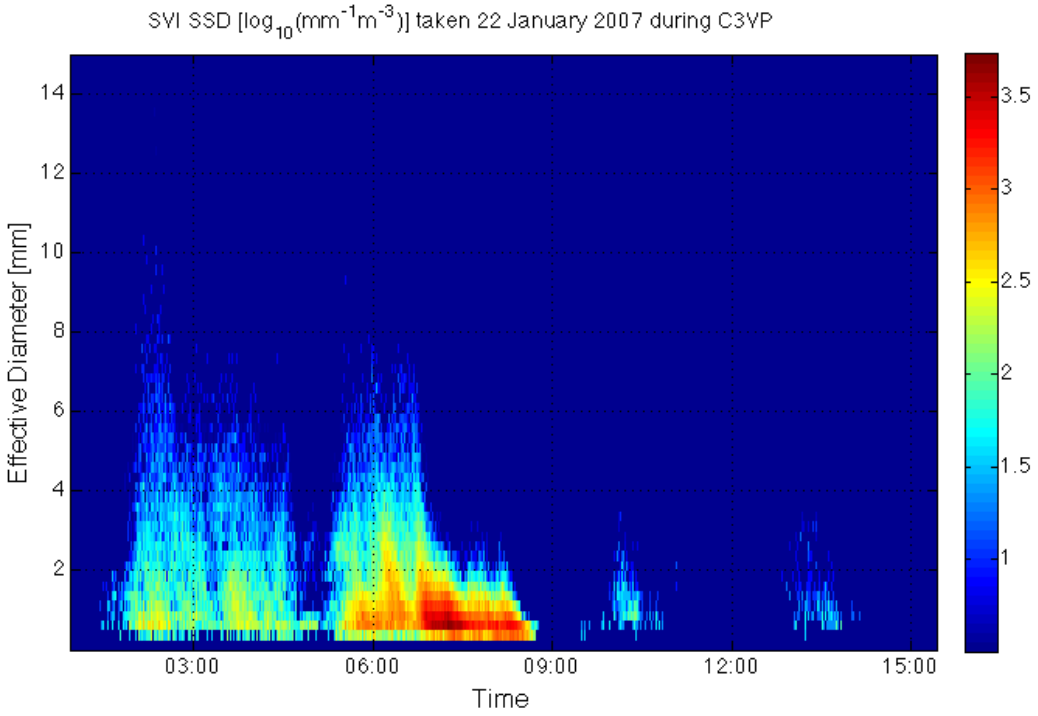

Figure 6.5: SSD taken by the SVI instrument during 22 January 2007 at the C3VP experiment

distribution (SSD) in units of [mm^{-1} m^{-3}]. The SSD product is defined as

$$SSD_i = \frac{N_i}{V_i dD} \tag{6.4}$$

where SSD_i is the Snow Size Distribution at diameter bin i, N_i is the number of particles found in that diameter bin, V_i is the measurement volume measured in m^3, and dD is the range of diameters included in the bin (measured in mm). Data taken by SVI during the C3VP experiment is shown in (6.5). The SSD data from the SVI instrument can be used to provide an estimation of the Median Mass-Weighted Diameter of the falling snow by using the cumulative distribution of mass over particle diameter and the definition

$$2\int_0^{D_0} D^3 N(D)\, dD = \int_0^{\infty} D^3 N(D)\, dD. \tag{6.5}$$

As the time resolution of the SVI data is significantly greater than that provided by AMFR and the line temporal resolution causes a higher variance in the measured distribution, the SSD retrieval from SVI is averaged into 10-minute bins before processing for comparison with the radar data. This had the effect of reducing random fluctuations in the data and in general caused the resulting distributions to more closely resemble an expected Gamma shape. Each time bin is processed as shown in Figure 6.6 to produce a time-series estimation of the SSD over the CARE cite during the C3VP experiment. The data from this instrument was used to validate the snow-size distribution measurements using AMFR's dual-wavelength ratio retrievals and the Meneghini model.

6.4 Comparison of Median Mass Diameter Retrievals

The ground truth provided by NASA Goddard Space Flight Center's Snow Video Imager was used to verify the SSD retrievals derived from AMFR's dual-wavelength ratio measurements.

6.4.1 Measurement volume

While both the SVI instrument and AMFR participated in the C3VP experiment, no particular effort was made to repeatedly scan AMFR over the SVI camera, as the radar continuously scanned storm features of interest. The consequence is that the scanned volume does not exactly match the SVI data, however due to the wide-spread nature of the event, it is expected that the scanned volumes at close range reasonably match the properties of the volume measured by the Snow Video Imager. A map of the relative location of the instruments is shown in Figure 6.7. It shows the relative location of AMFR and SVI, along with the footprint of the scanned volume. As AMFR would continuously focus on the heart of the storm, individual PPI scans only incorporate a portion of the shown area.

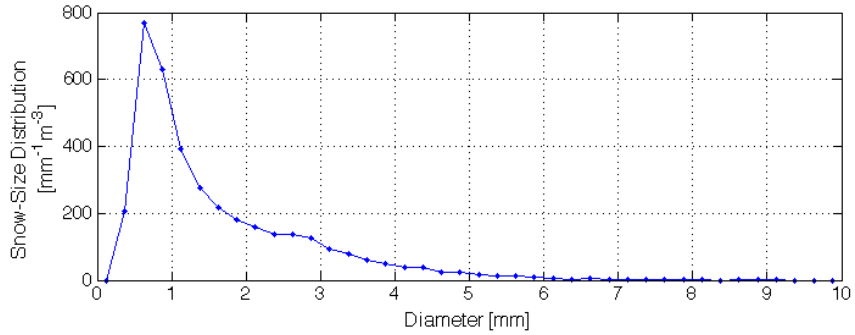

(a) Sample SVI Snow-Size Distribution Retrieval

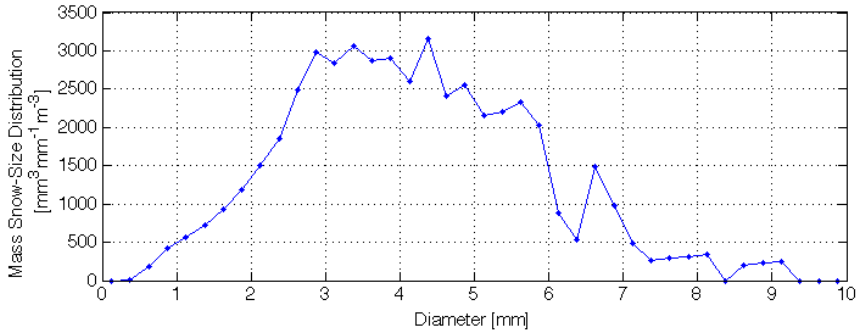

(b) Mass Snow-Size Distribution Retrieval

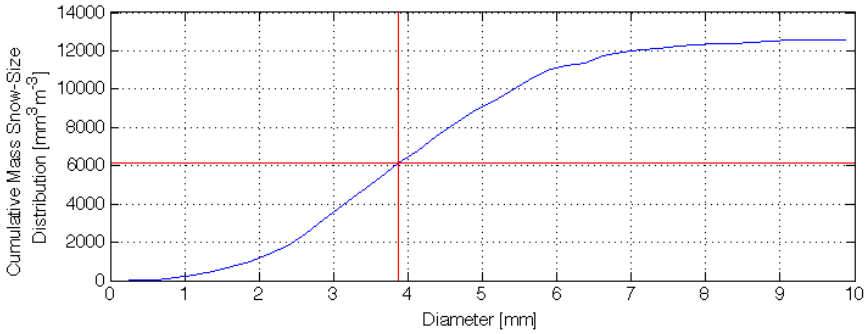

(c) Cumulative Mass Snow-Size Distribution Retrieval

Figure 6.6: A sample of SVI data showing the SSD, Mass-Weighted SSD, and Cumulative Mass-Weighted SSD. Subplot (c) also shows the resulting Median Mass Diameter of 3.88mm.

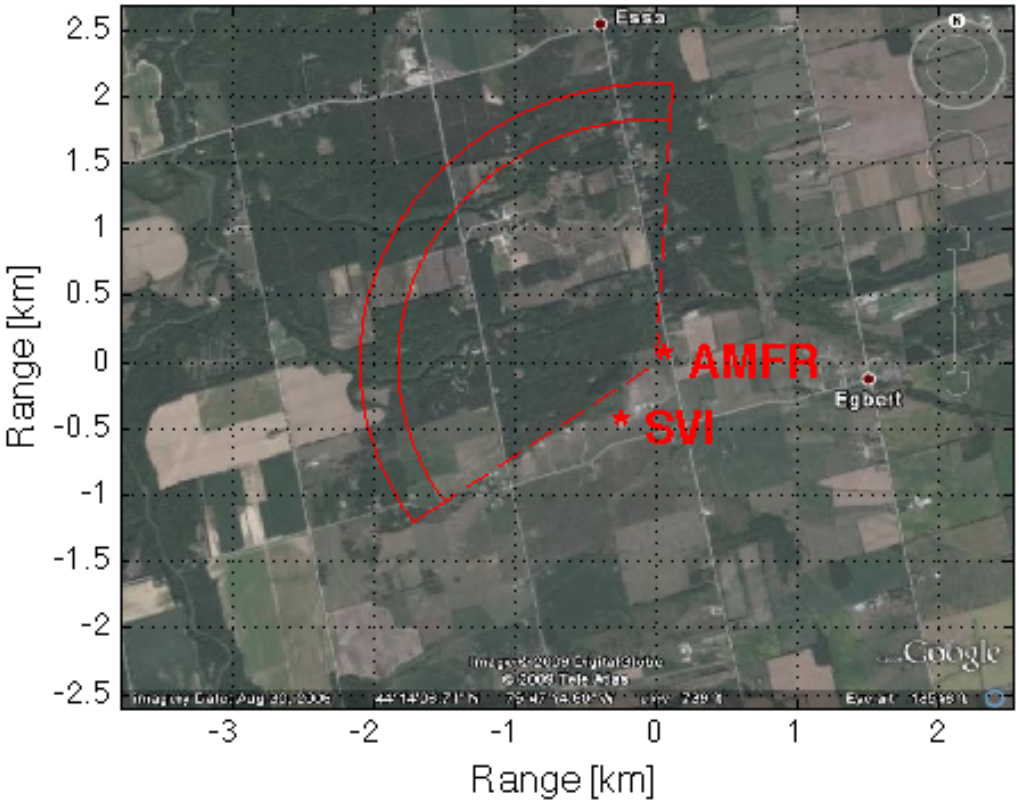

Figure 6.7: The location of AMFR and SVI during the C3VP experiment. The volume used in the AMFR D_o retrievals is shown. The image is taken from Google Earth and is (c) DigitalGlobe and (c) Tele Atlas

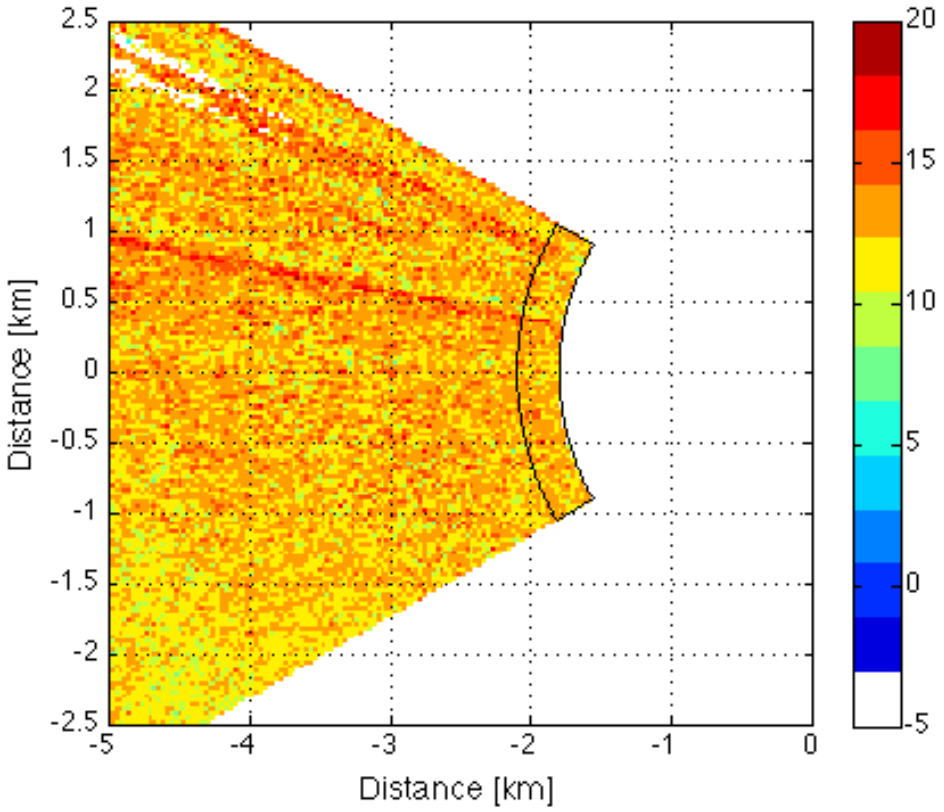

Figure 6.8: A close of DWR data [dB] from the part of a PPI scan used to estimate precipitation snow-size distribution. The averaged area shown with a black outline.

The area used for this comparison is shown in Figure 6.8. The part of the scan used for this comparison is outlined in black, and is a subset of the area shown in Figure 6.7. Figure 6.8 demonstrates the relatively uniform nature of the DWR data from this winter storm. It also shows that the individual data points have a moderate amount of variance. This is a function of the integration time, range resolution, and the largely random shapes of individual snowflakes. The modifications made to the transmit and receive scheme will improve this by effectively doubling the integration time for the same scanning speed.

Several streaks of high DWR can be seen in Figure 6.8. These are caused by ground clutter near the radar blocking the Ka-band signal more than the Ku-band.

Due to this, a median average was used over the rays so as to minimize the impact of these few large outliers.

6.4.2 Direct SSD Comparison

The time-series Median Mass Diameter retrieval near the CARE site from AMFR's DWR data can be compared with the ground truth derived from the size spectrum measurement from the SVI. The data are shown in Figure 6.9, along with the difference between the two instruments' retrievals. For an image of the size spectrum measured by the SVI during this time, please refer to Figure 6.5.

As can be seen in Figure 6.9, the SSD retrieval from AMFR's PPI scans closely follow those obtained by the Snow Video Imager. This provides credence to the data provided by AMFR in combination with the Meneghini model. As such, these are the first experimentally verified SSD retrievals from a Ku-Ka band radar's DWR data during a winter storm.

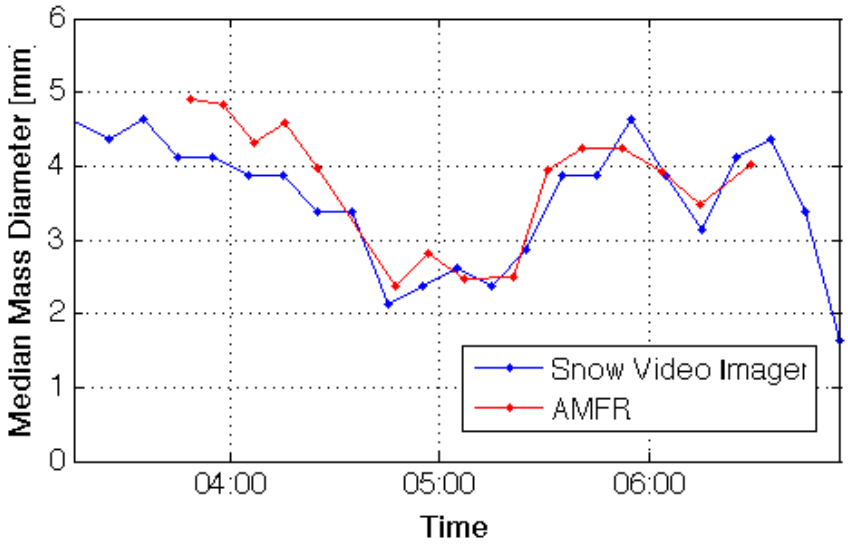

(a) Snow Size Distribution retrievals (mm)

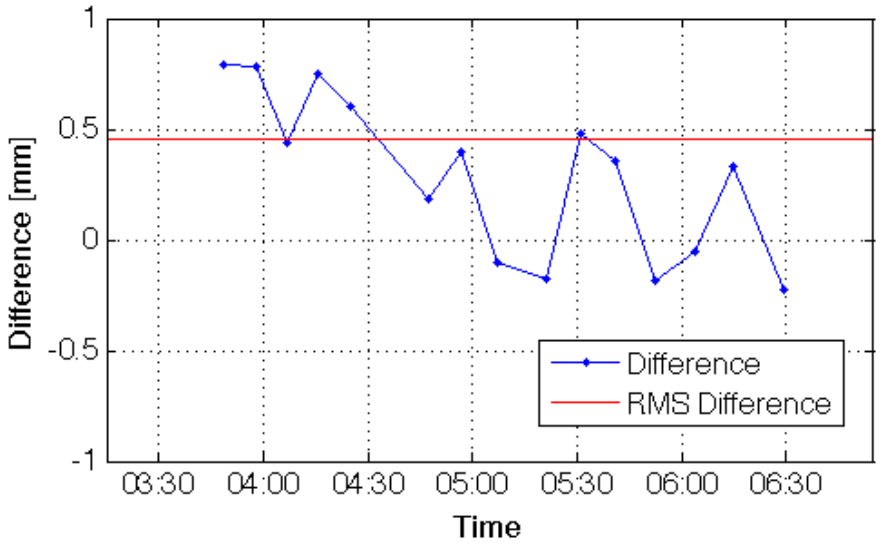

(b) Retrieval difference (mm) interpolated to AMFR's scans

Figure 6.9: A comparison of the precipitation snow-size distribution retrieval from the Snow Video Imager and AMFR's dual-wavelength ratio data

CHAPTER 7

CONCUSIONS AND FUTURE WORK

The UMass Microwave Remote Sensing Laboratory's Advanced Multi Frequency Radar successfully produced reflectivity and dual-wavelength ratio measurements during a synoptic winter storm event during the 2007 Canadian CloudSat/CALIPSO Validation Project in Ontario. Despite hardware difficulties resulting in a poor initial calibration, an internal calibration approach was able to recover the data.

The resulting DWR data was used with a scientific model to produce estimations of the median-mass diameter of snowfall. This result was compared with the products from a nearby ground-based video instrument to provide confirmation of the results. This was one of the first measurements of its kind with access to ground-truth, and showed very good agreement between the two instruments in median-mass diameter.

7.1 Summary of Achievements

Work by the author on AMFR began one year after the C3VP experiment. Accomplishments leading to this document are as follows, and include every step in the transformation of uncalibrated data into precipitation microphysics retrievals.

1. Determined and corrected the cause of the initially poor calibration in the data produced by AMFR during the 2007 C3VP experiment. Part of the problem was found to be damaged components in the RF section, which were replaced.

2. Developed and implemented an internal calibration of the system that allowed for the calibration of the C3VP data to be corrected while providing an accurate

way of accounting for the pulse compression gain and system gain variations. Scientific data produced through this calibration was evaluated by Colorado State University and found to be suitable for further scientific work.

3. Used Doppler data and successive RHI scans to remove the effects of relative clock drift between the positioner and radar data caused by the extreme temperature difference between the two data computers.

4. Used the Ka- and W-band systems to produce high power RF energy for a microwave absorber test in a controlled laboratory setting.

5. Modified the pulse scheme and data acquisition system to produce differential phase data while simultaneously decreasing measurement uncertainty by increasing the effective data integration time for each polarization.

6. Applied AMFR dual-wavelength data to the results of a scientific model to provide an estimate of median-mass diameter of snowfall during a winter storm event at the C3VP experiment. These results were then compared to nearby ground-data and were found to be in good agreement.

7.2 Suggested Future Work

While AMFR has had a successful field experiment and has produced interesting scientific data, work remains in both analyzing the scientific data from C3VP and in future upgrades, repairs, and deployments.

7.2.1 Analysis of C3VP Scientific Data

While some interesting results utilizing AMFR's dual-wavelenth ratio data for drop-size distribution retrievals were demonstrated in this document, the author is not a scientist by training and believes that significant contributions can still be

made using existing data from C3VP. In particular, the following approaches are recommended:

1. Derive estimations of total snow mass and particle density from AMFR's dual-wavelength ratio and reflectivity data for different values of μ in the Gaussian distribution and different snow densities.

2. Now that dual-wavelength ratio data has been shown to produce reasonable estimations of the median-mass diameter of snowfall near the CARE site, use DWR data contained in the extended ranges of PPI and RHI scans to obtain information about particle sizes and equivalent liquid water content over entire scans. This should provide information about the structure and microphysics of the storm.

7.2.2 Tasks for System Improvement and Deployment

It is hoped by the author that the AMFR system will be used for future scientific data retrievals in preparation for the upcoming NASA Global Precipitation Measurement mission. In particular, it would be useful to gather dual wavelength ratio data of rain, again in conjunction with a ground based instrument for determining drop-size distribution and liquid water content.

Future deployments of the AMFR system are dependent on some hardware upgrades and modifications. The following tasks are of varying importance, but all should provide significant upgrades to the system and its ability to collect valuable scientific data.

1. Determine the cause of the W-band klystron failure. In the event that it is determined that the failure was caused by reflections from arcing in the latching circulator network (before this network was removed), then replace the klystron with either a new or used tube while retaining the current modulator. In the

even that it is determined that the klystron failed due to an over-duty or over-voltage problem, consider options for replacing both the modulator as well as the klystron to avoid damage to future tubes.

2. Insert isolators directly after the klystron tubes in both the Ku- and Ka-band systems to avoid similar damage to the high-power tubes from any failures in the switching and polarization networks.

3. Improve the mechanical stability of the waveguide RF-components in the Ka-band system to reduce flexing that could cause reflections or calibration drifts.

4. Insert an additional latching circulator in the calibration paths to increase the calibration signal to transmit leakage ratio and reduce the uncertainty of calibration from in- and out-of phase interference from the leaked signal.

7.3 Conclusion

AMFR is a powerful system that incorporates many of the latest advances in state-of-the-art radar remote sensing. It accomplishes good sensitivity in a mobile platform by incorporating high-power klystron amplifiers and pulse compression. It achieves flexible polarization data through a polarization diversity scheme. In addition, it is one of only a few Ku-Ka band multi-frequency radars, and should the W-band transmitter be repaired, it will be the only three frequency (Ku-Ka-W) band radar in existence for climate and weather research.

With these advances comes a complex instrument with the difficulties found in all such instruments. The choice of high-power klystron amplifiers produces excellent sensitivity and range at the cost of increased risk from the high-voltage systems. The choice of multiple frequencies for cutting edge microphysics research comes at the cost of incorporating three separate transmitters and RF receivers as well as complexity in synchronizing the different frequencies.

With these risks can come scientific data unlike what is available from other existing radar systems. The C3VP data, despite the hardware difficulties experienced, shows that two-frequency data can be useful for measuring the drop-size distribution of snowfall using existing models. It is hoped that the addition of differential phase measurements as well as a third higher frequency will result in a far greater wealth of scientific information.

The current challenges facing the AMFR instrument are small compared to the wealth of scientific information it is capable of producing. The author strongly hopes that with relatively minor additional support, the system will be producing strong scientific three-frequency data to produce cloud and precipitation microphysics research as well as support to GPM and other satellite instruments.

APPENDIX

ADDITIONAL C3VP DATA

A sample of data during the 22 January 2007 storm is shown here. Additional RHI scans from this storm are also available.

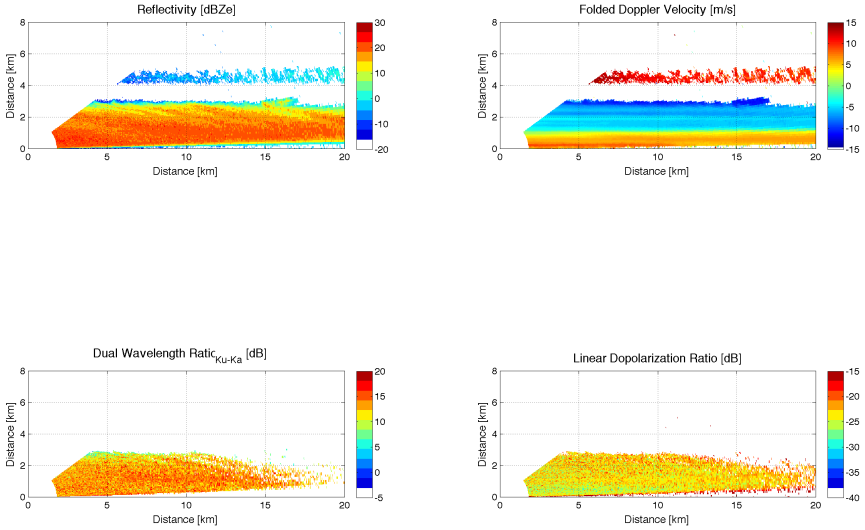

Figure A.1: C3VP Data, 22 January 2007, 3:42

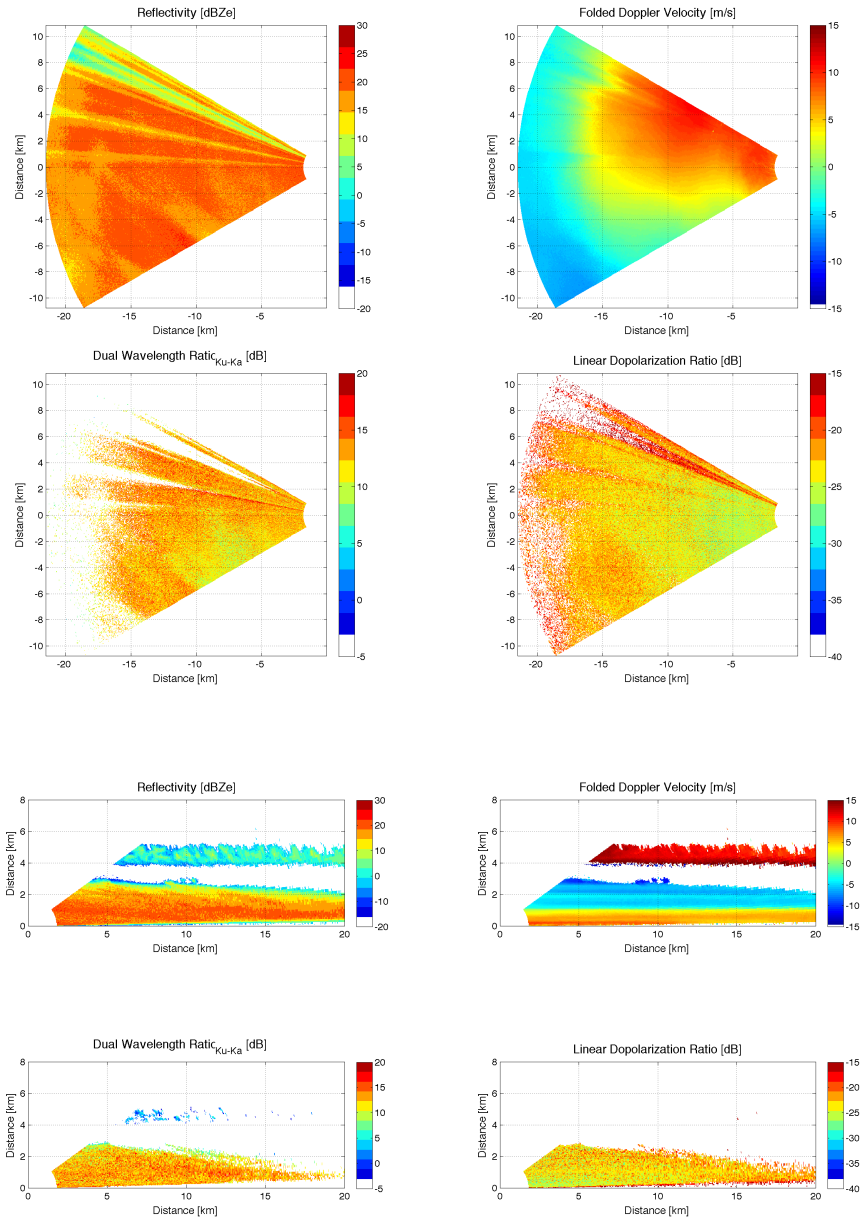

Figure A.2: C3VP Data, 22 January 2007, 3:48

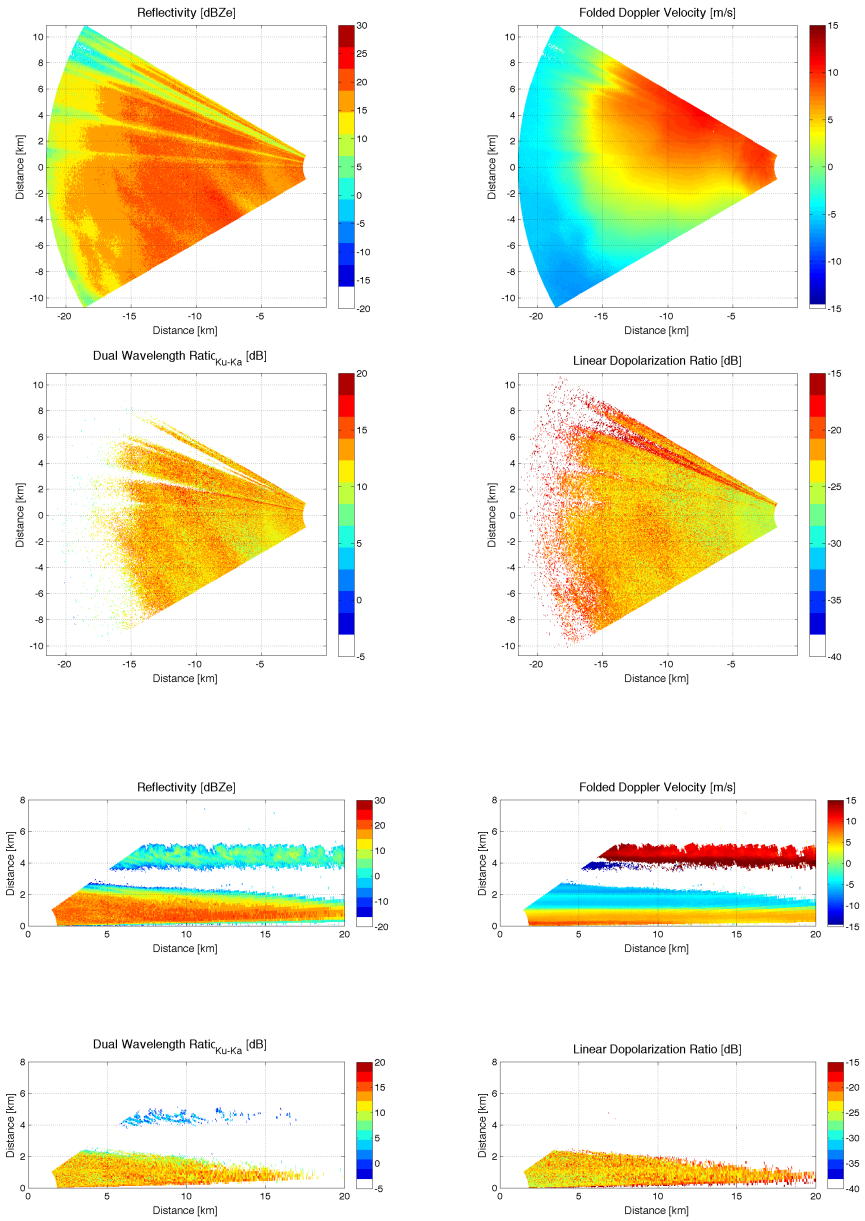

Figure A.3: C3VP Data, 22 January 2007, 3:57

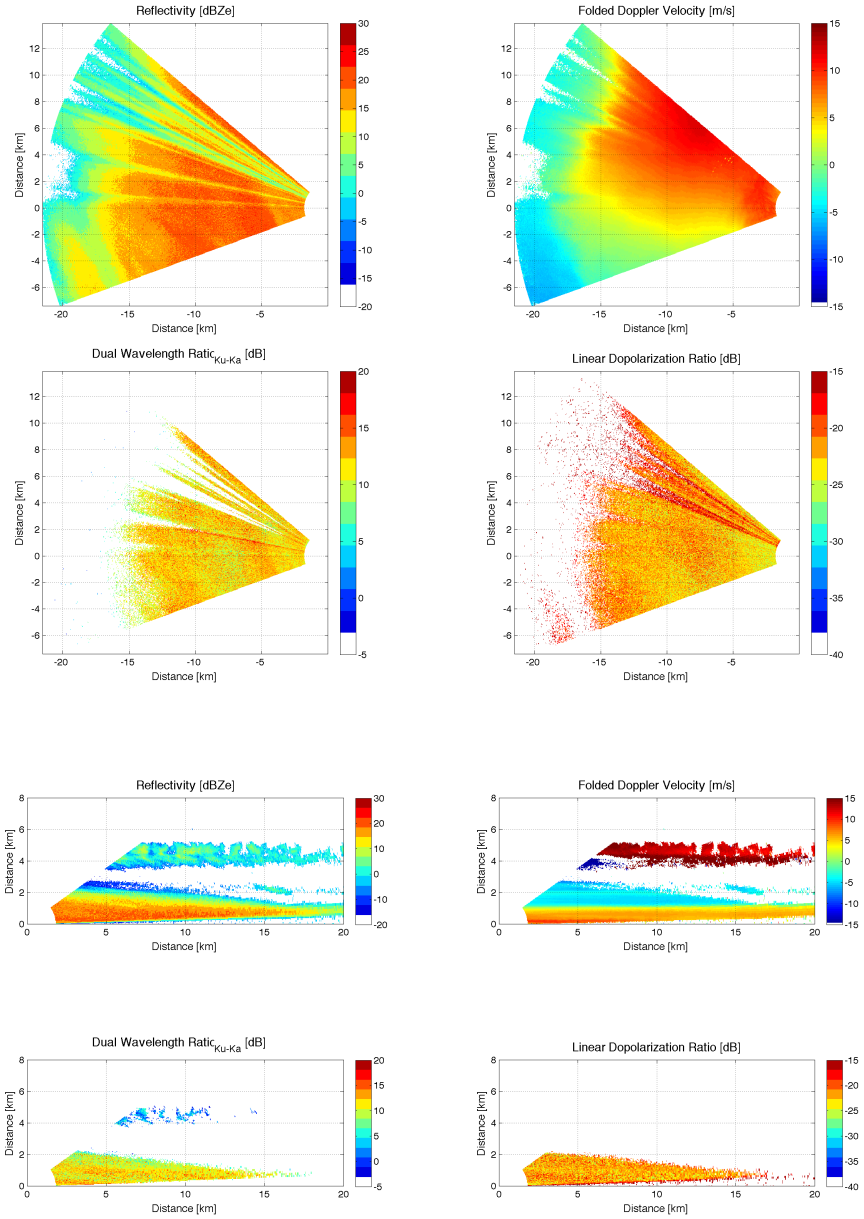

Figure A.4: C3VP Data, 22 January 2007, 4:06

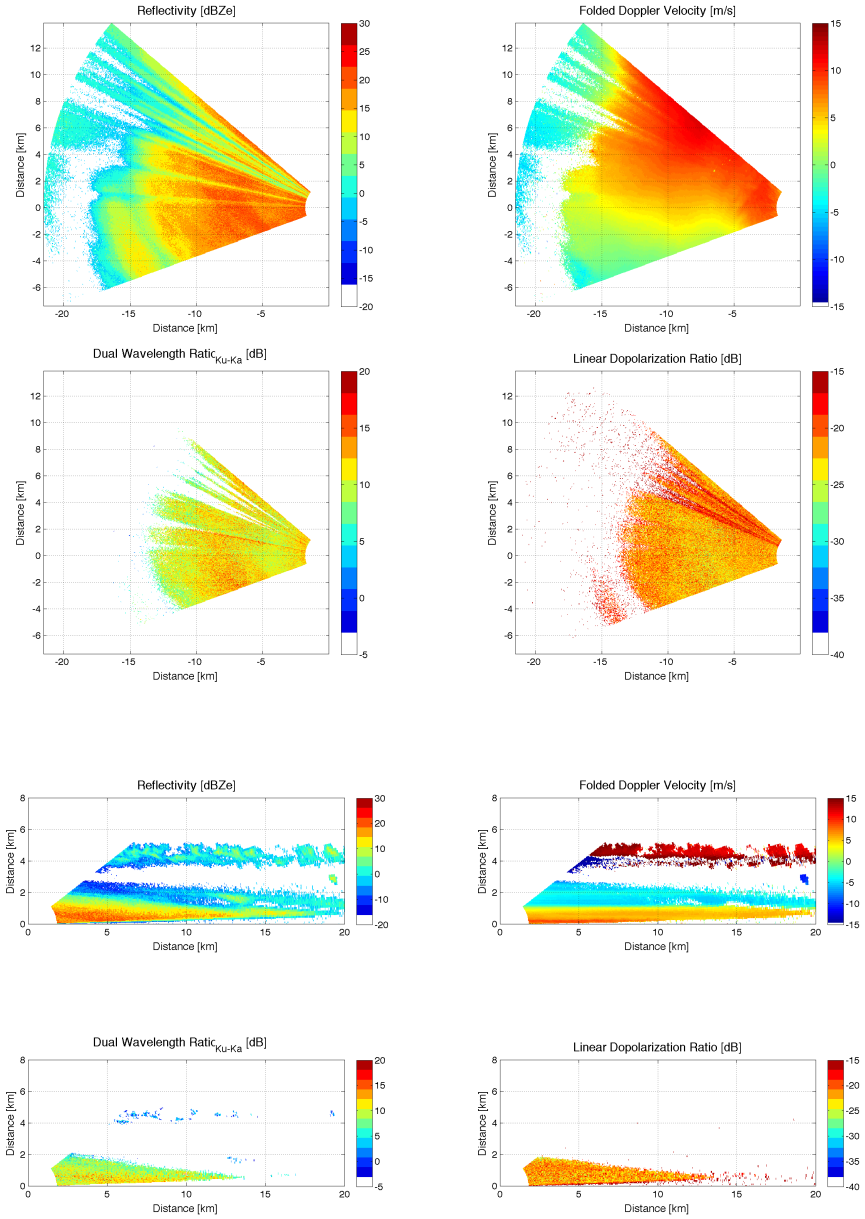

Figure A.5: C3VP Data, 22 January 2007, 4:15

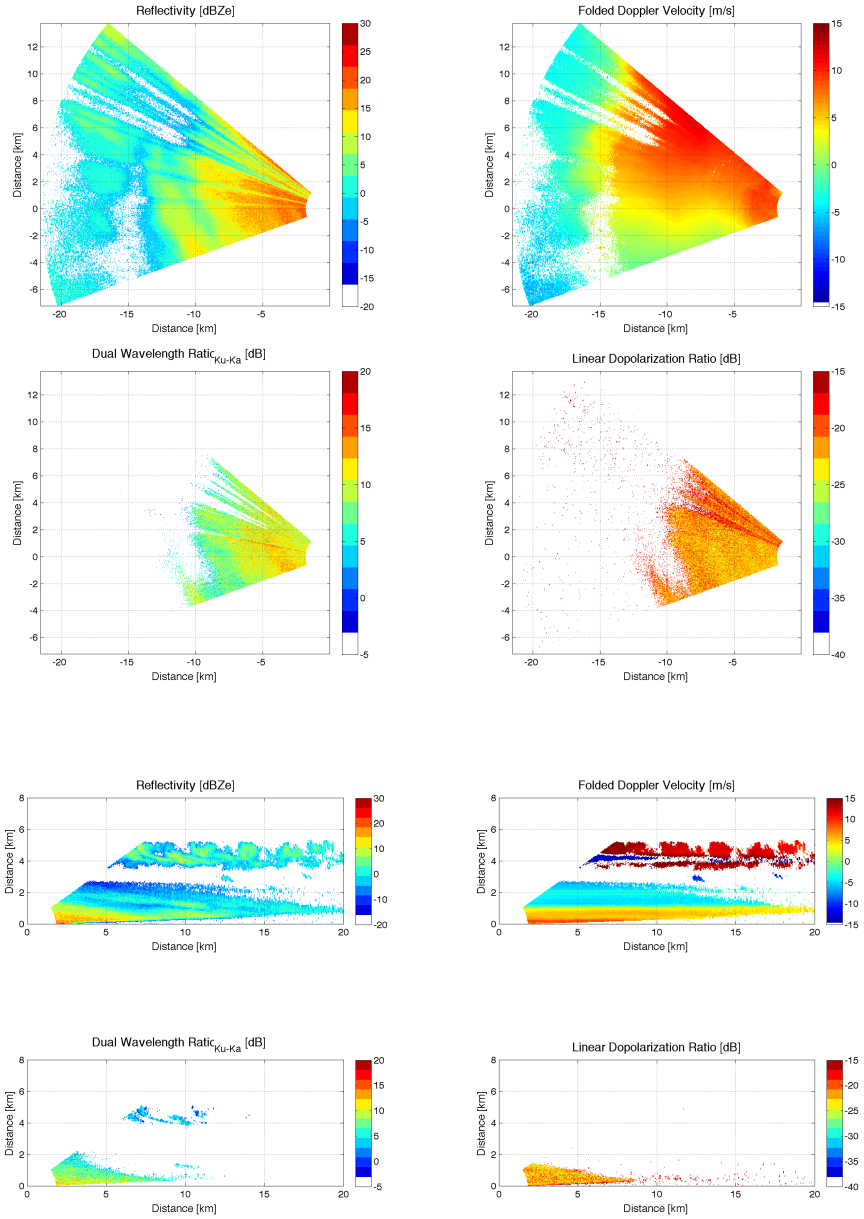

Figure A.6: C3VP Data, 22 January 2007, 4:25

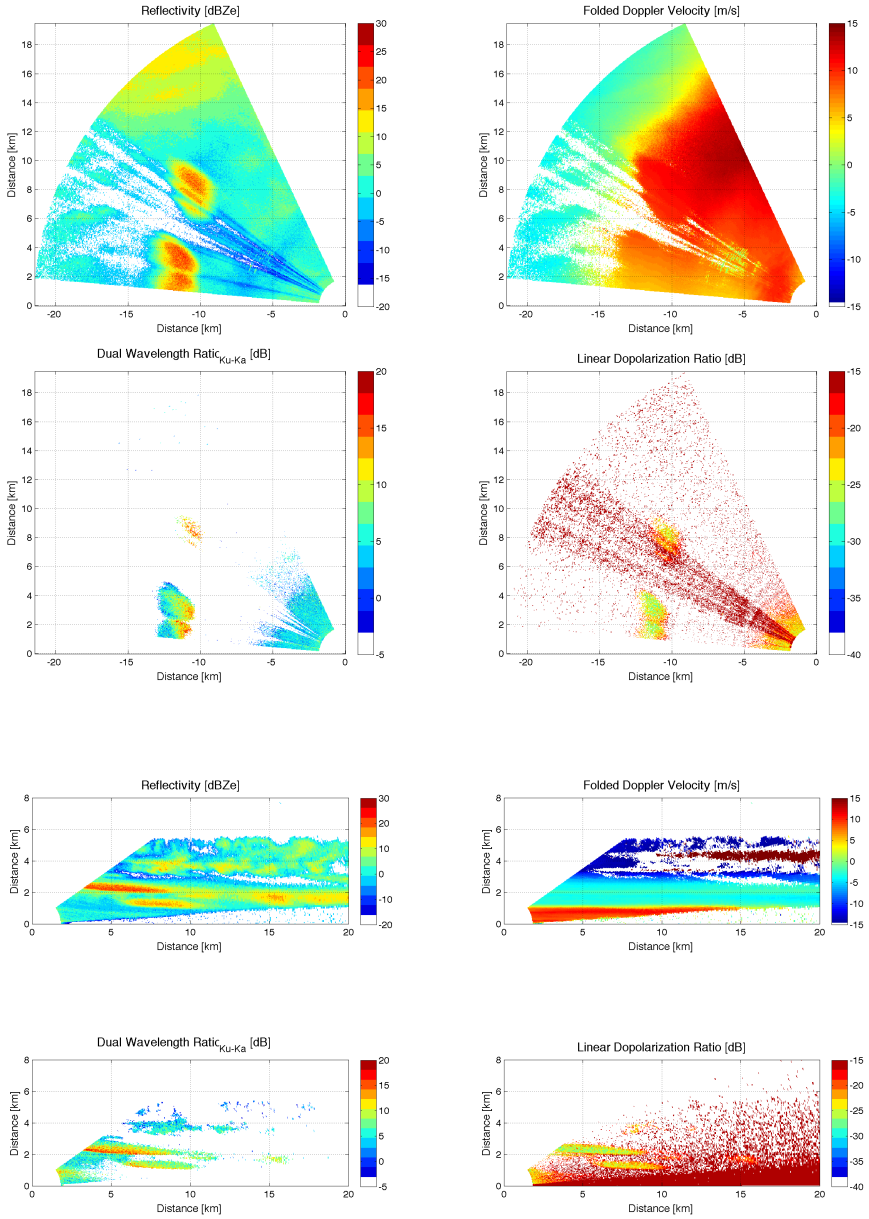

Figure A.7: C3VP Data, 22 January 2007, 4:47

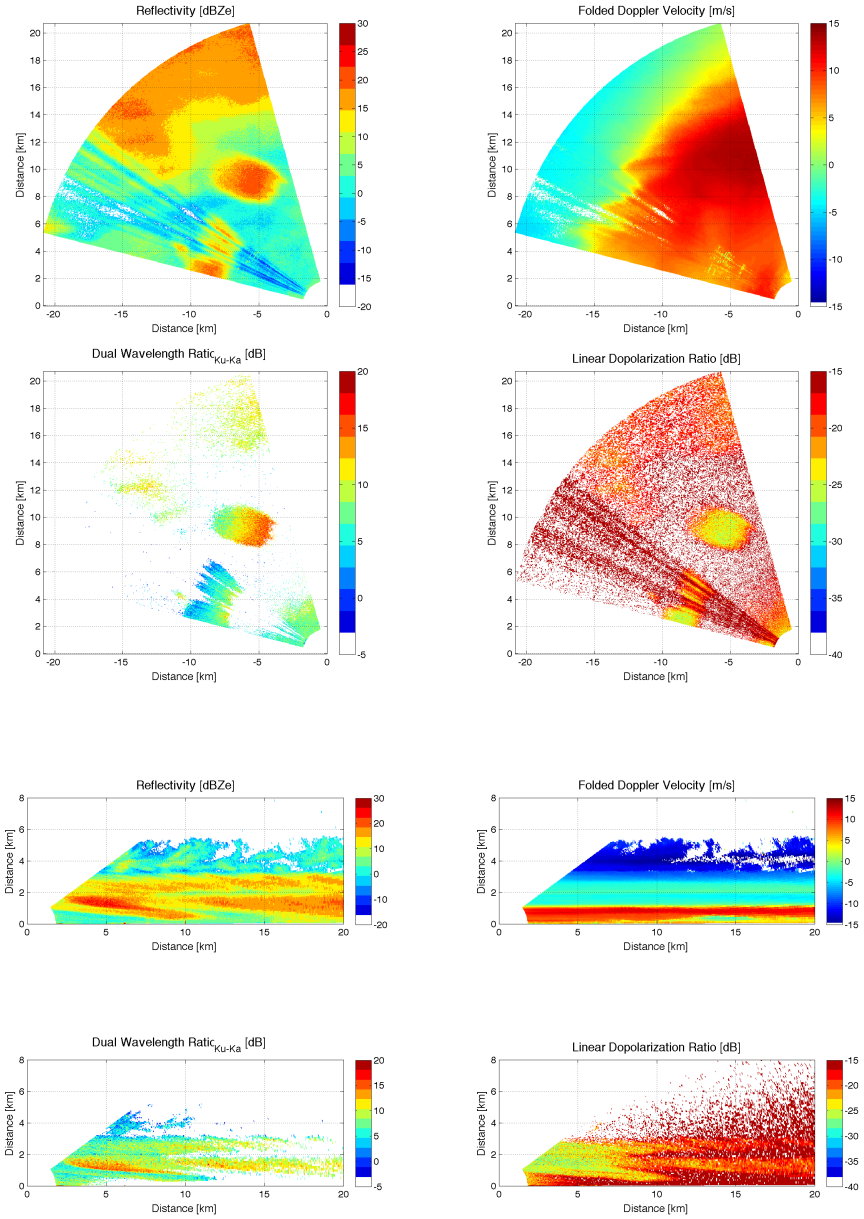

Figure A.8: C3VP Data, 22 January 2007, 4:56

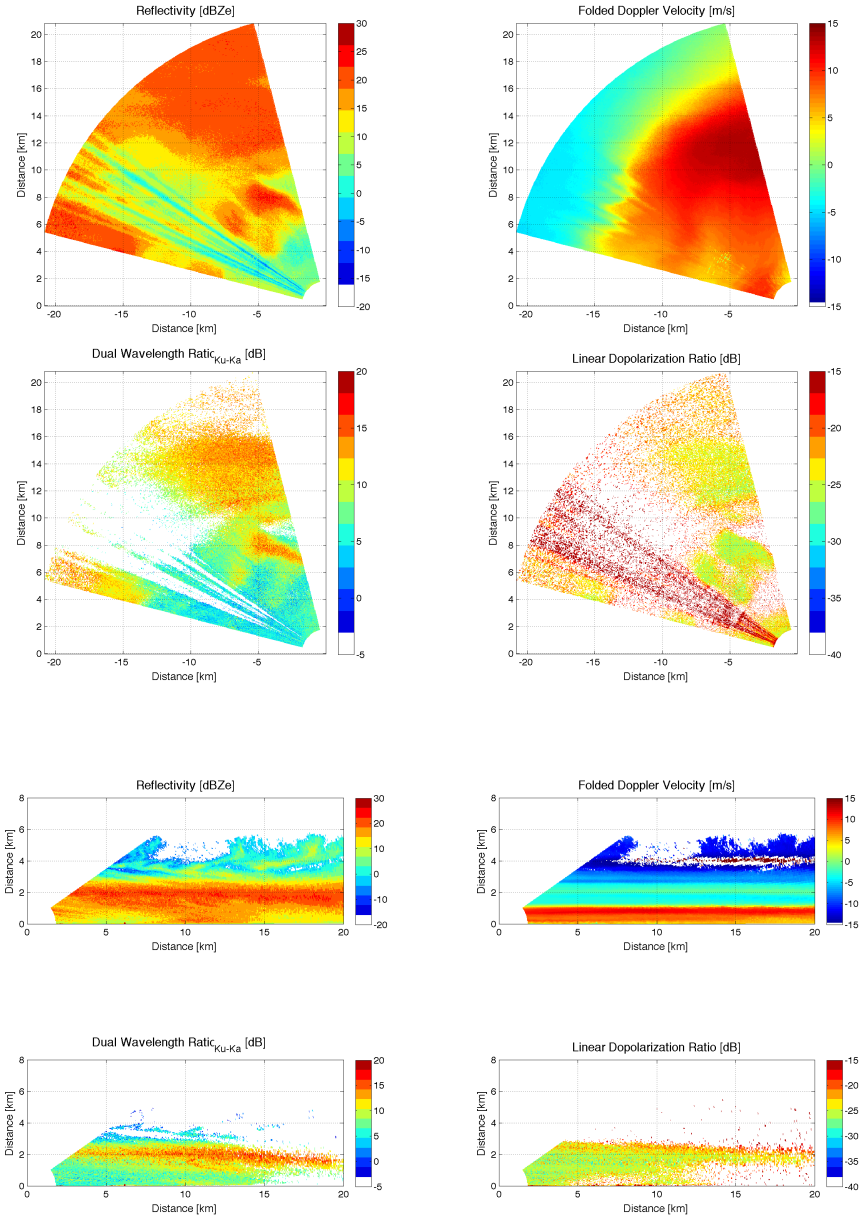

Figure A.9: C3VP Data, 22 January 2007, 5:06

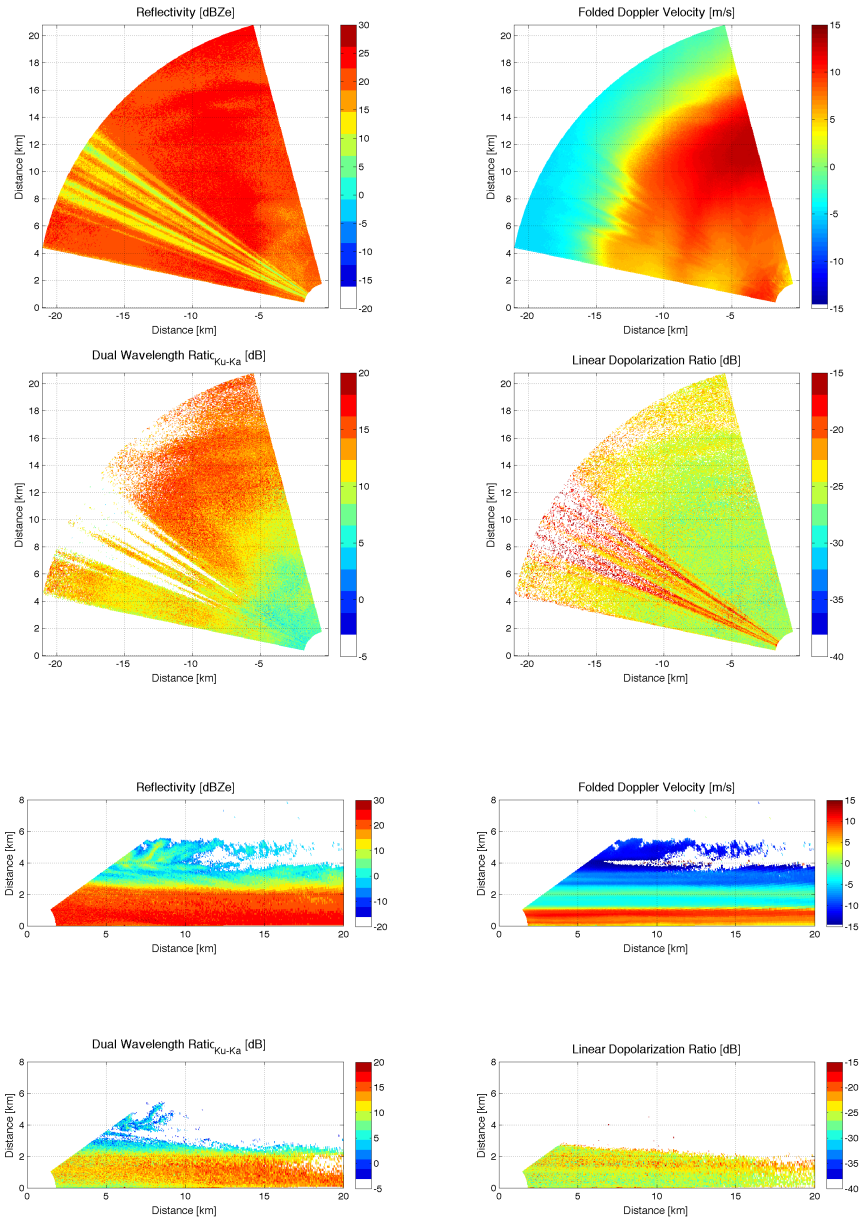

Figure A.10: C3VP Data, 22 January 2007, 5:20

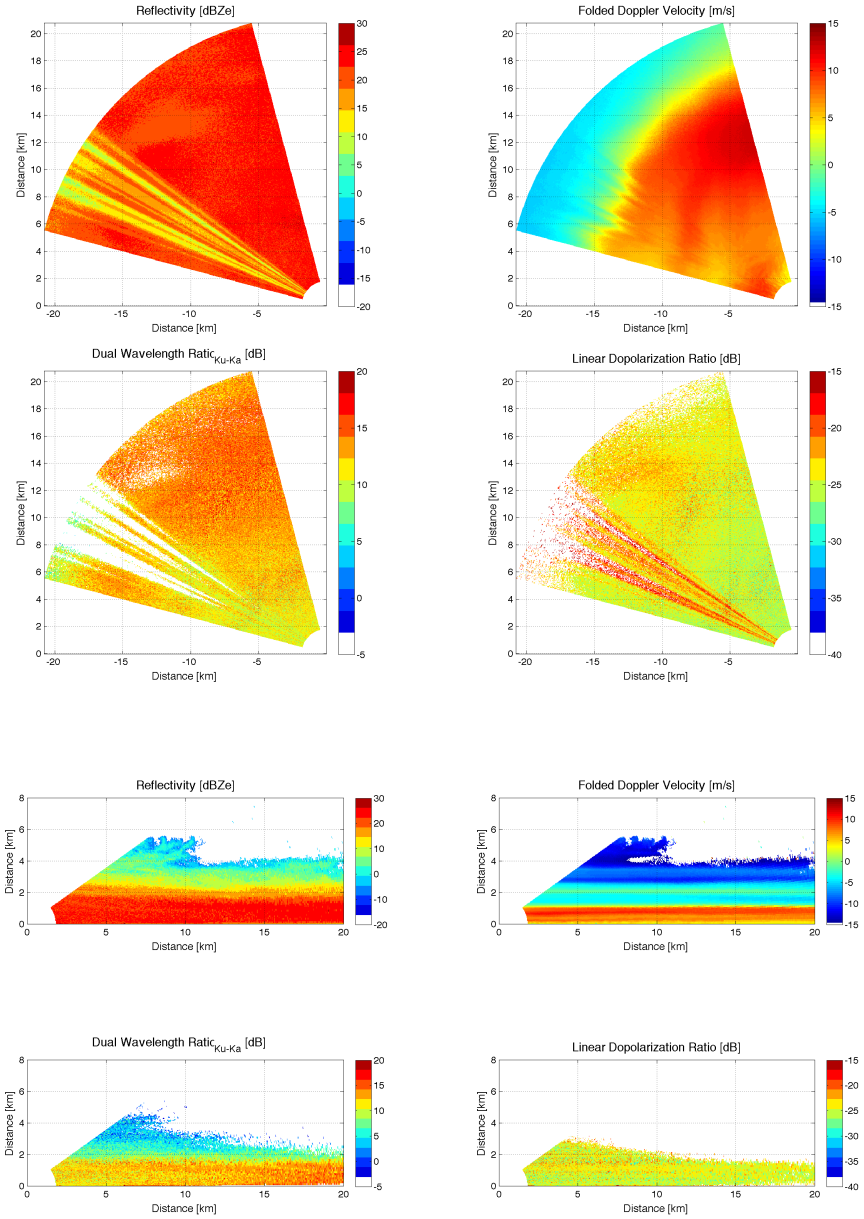

Figure A.11: C3VP Data, 22 January 2007, 5:31

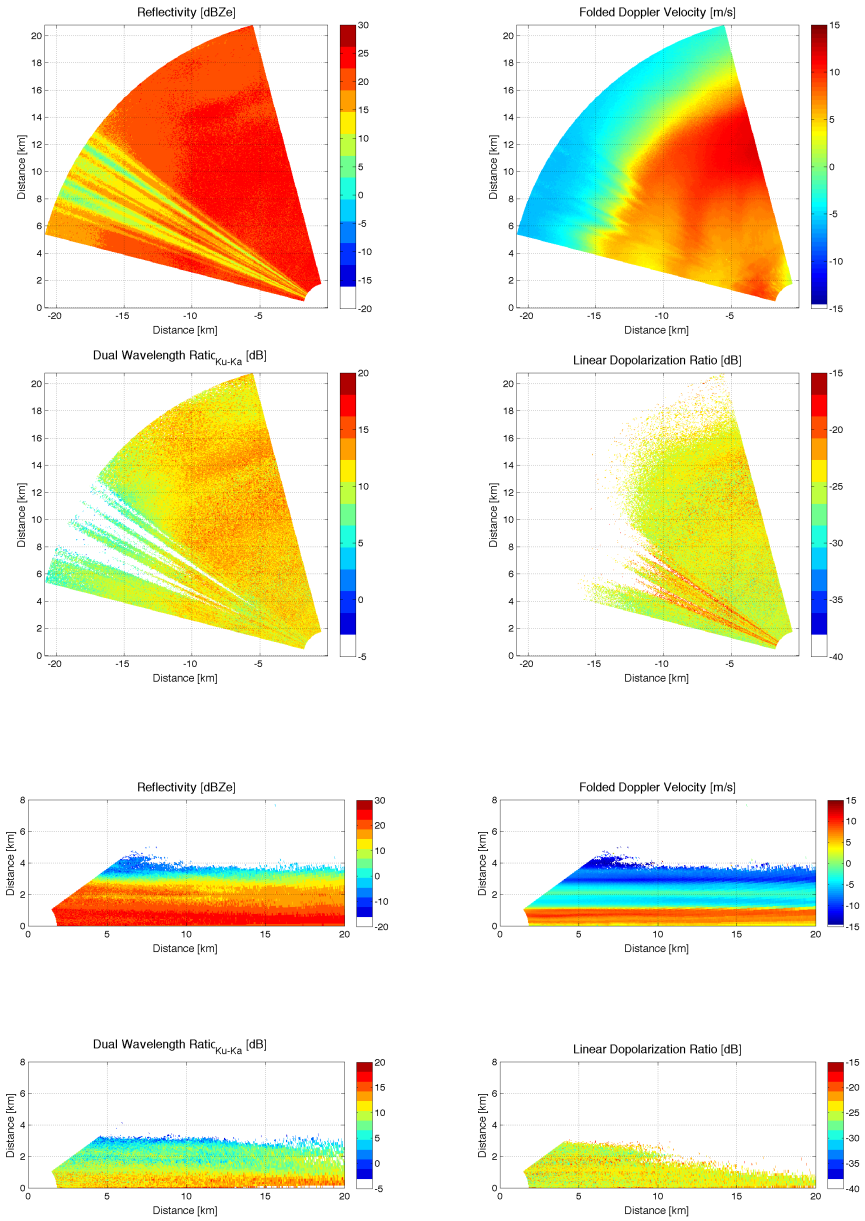

Figure A.12: C3VP Data, 22 January 2007, 5:40

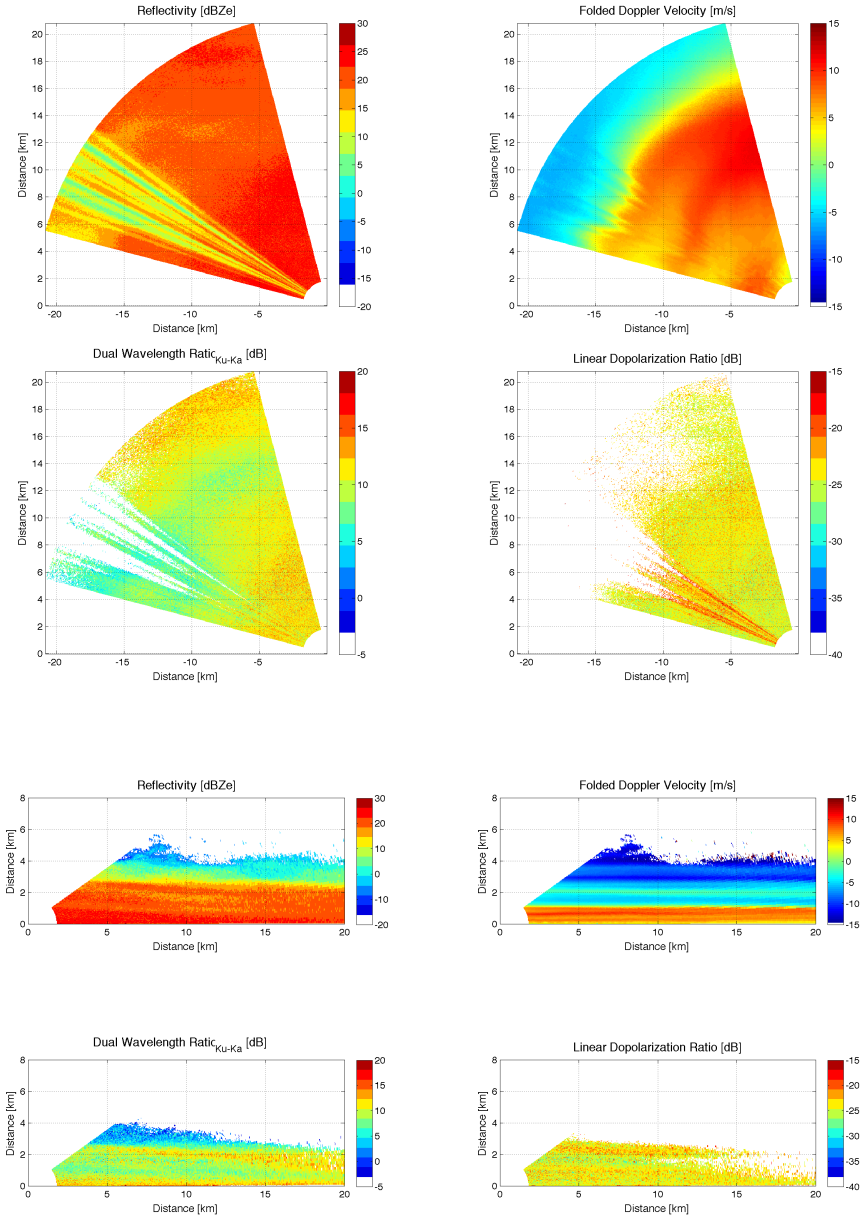

Figure A.13: C3VP Data, 22 January 2007, 5:52

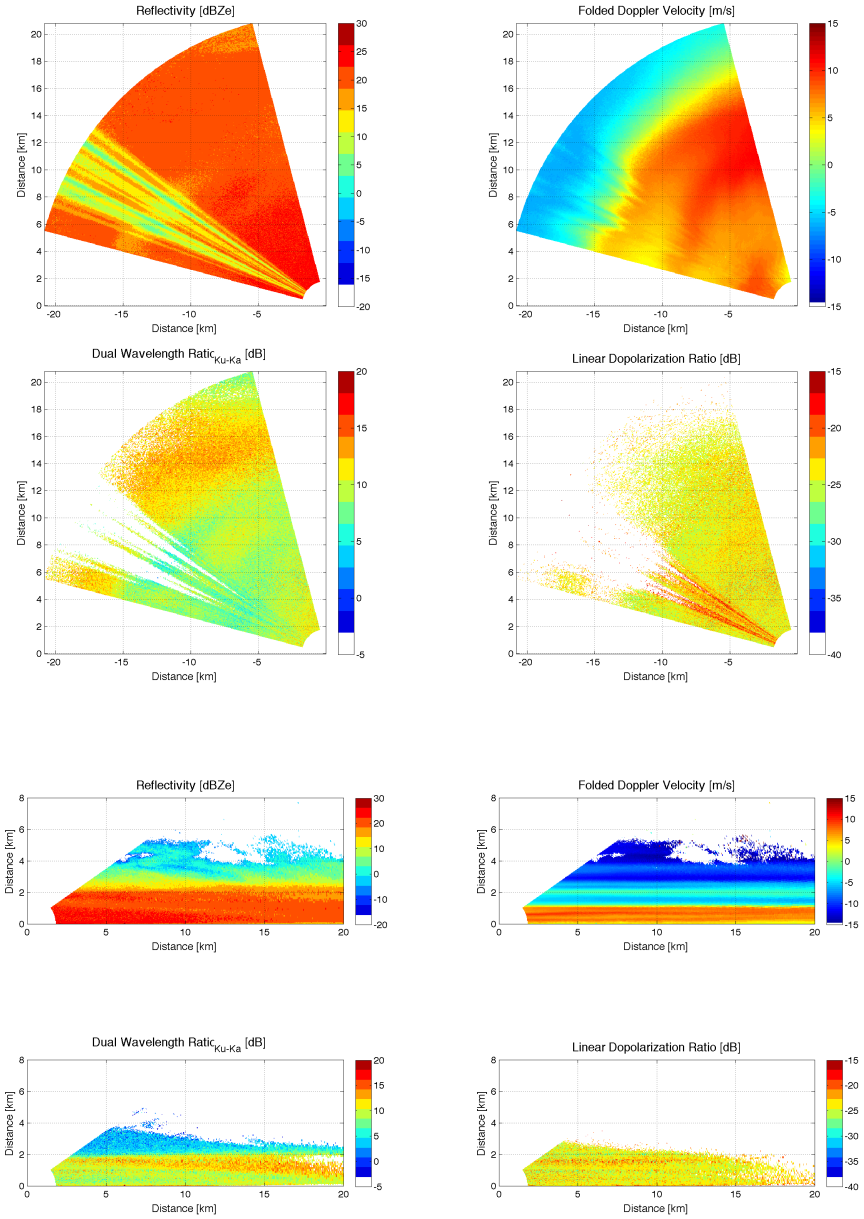

Figure A.14: C3VP Data, 22 January 2007, 6:03

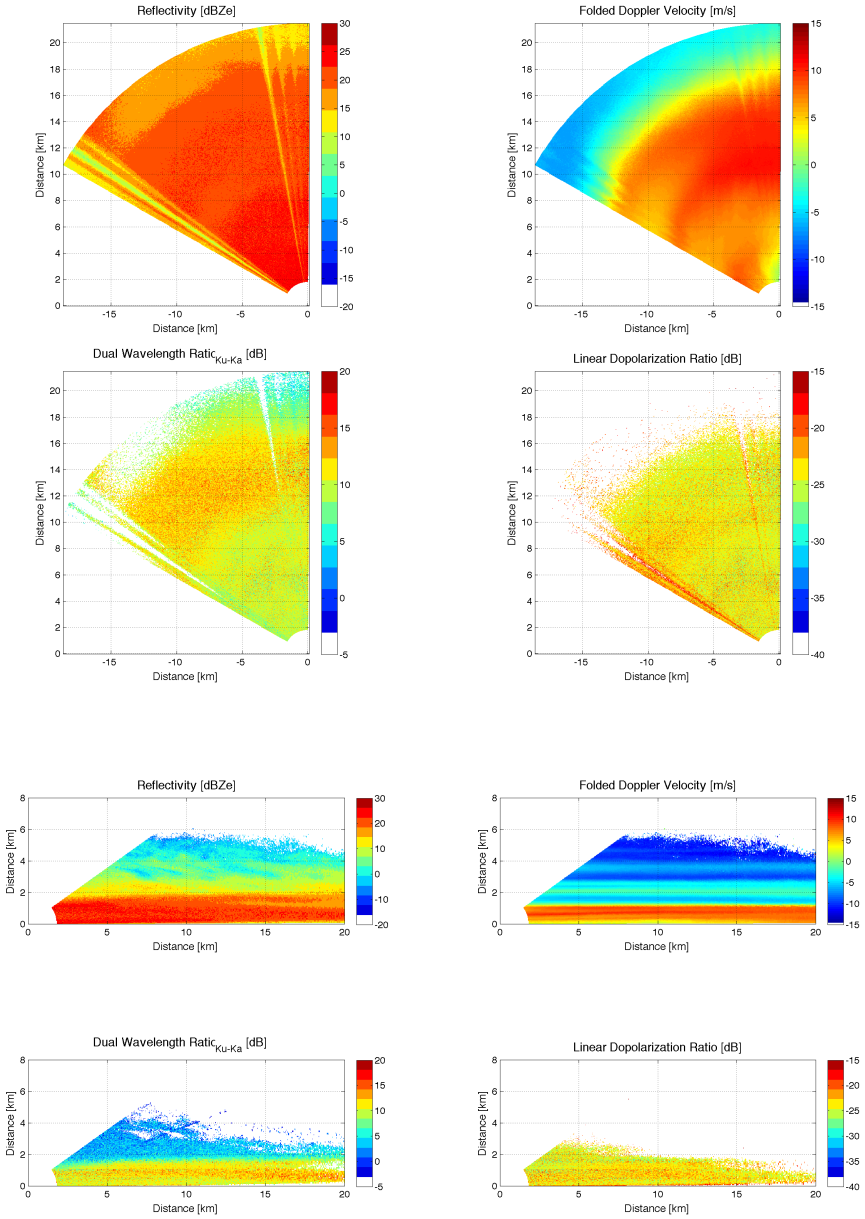

Figure A.15: C3VP Data, 22 January 2007, 6:14

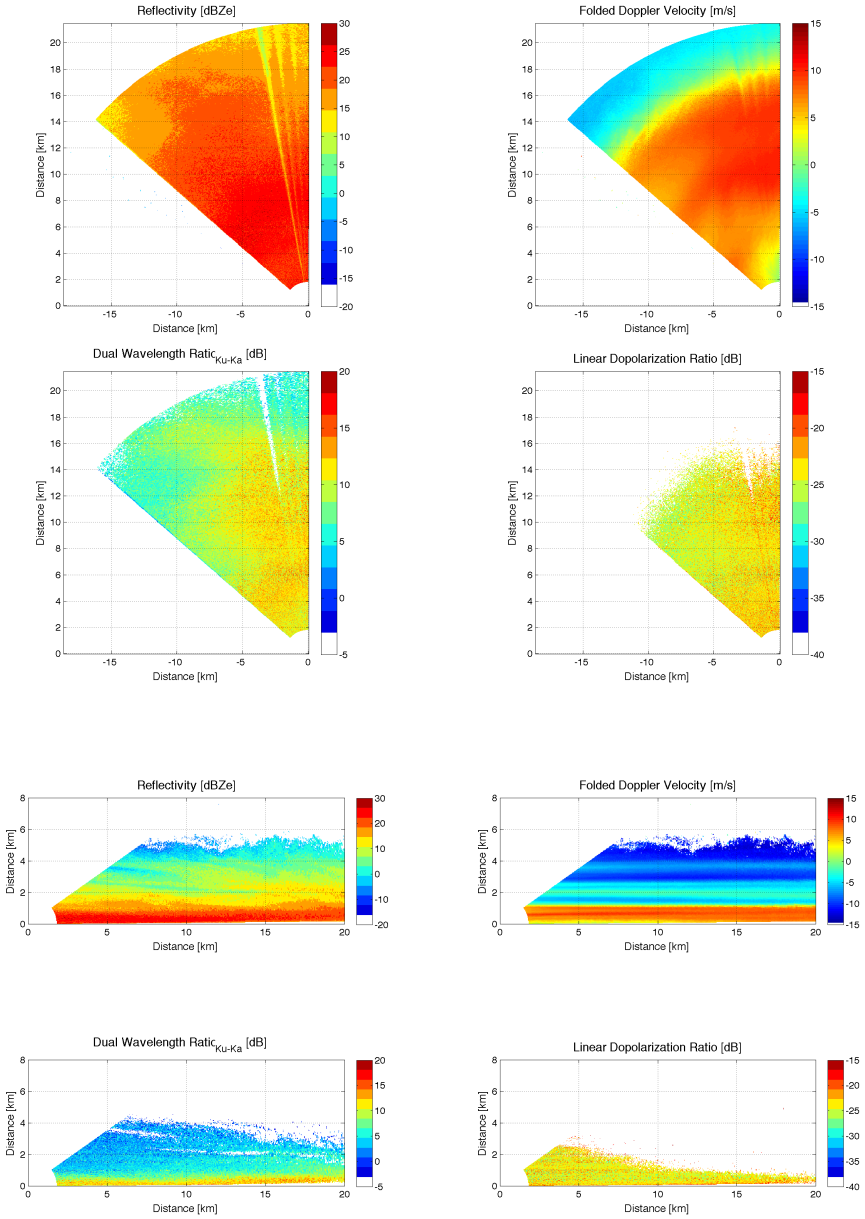

Figure A.16: C3VP Data, 22 January 2007, 6:29

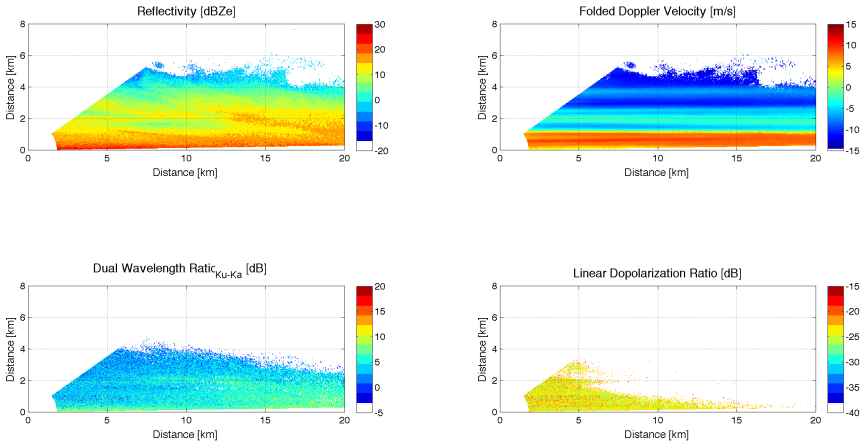

Figure A.17: C3VP Data, 22 January 2007, 6:41

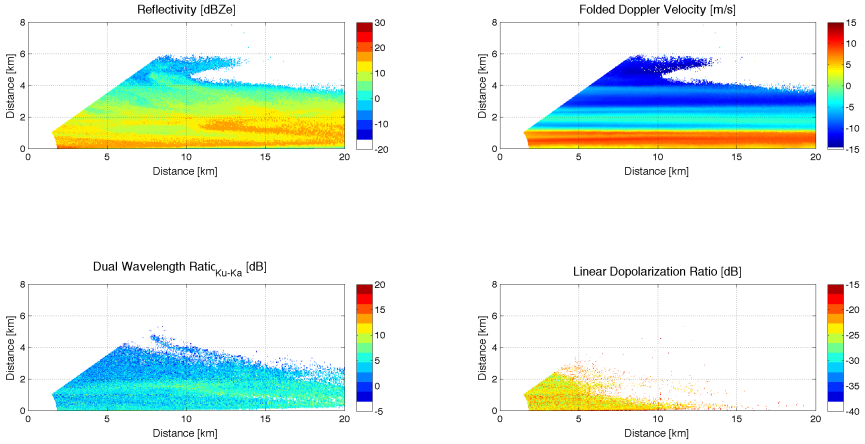

Figure A.18: C3VP Data, 22 January 2007, 6:50

BIBLIOGRAPHY

[1] Bringi, V. N., and Chandrasekar, V. *Polarimetric Doppler Weather Radar: Principles and applications*. Cambridge University Press, 2001.

[2] Doviak, Richard J., and Zrnic, Dusan S. *Doppler Radar and Weather Observations*. Academic Press, San Diego, California, 1984.

[3] Liao, Liang, Meneghini, Robert, Iguchi, Toshio, and Detwiler, Andrew. Use of dual-wavelength radar for snow parameter estimates. *Journal of Atmospheric and Oceanic Technology 22* (April 2005), 1494–1506.

[4] Majurec, Ninoslav. *Advanced Multi-Frequency Radar: Design, Preliminary Measurements and Particle Size Distribution Retrieval*. PhD thesis, University of Massachusetts, 2008.

[5] Marshall, J. S., and Palmer, W. McK. The distribution of raindrops with size. *Journal of Atmospheric Sciences 5* (August 1948), 165–166.

[6] McLinden, Matthew L., Majurec, Ninoslave, and Siqueira, Paul. Calibration of the UMass Advanced Multi-Frequency Radar (AMFR). In *IEEE Geoscience and Remote Sensing Symposium* (2008).

[7] Newman, Andrew J., Kucera, Paul A., and Bliven, Larry F. Presenting the snowflake video imager (SVI). *Journal of Atmospheric and Oceanic Technology 26* (February 2009), 167–179.

[8] Petersen, Walt, Lang, Tim, and Jackson, Gail. C3VP science logs, 2007. `https://radarmet.atmos.colostate.edu/elog/C3VP/22`.

[9] Sachidananda, M, and Zrnic, D.S. Efficient processing of alternately polarized radar signals. *Journal of Atmospheric and Oceanic Technology 6* (February 1989), 173–181.

[10] Skolnik, M. I. *Radar Handbook*, 2 ed., vol. 2. McGraw-Hill, Boston, Massachusetts, 1990.

[11] Ulaby, Fawwaz T., Moore, Richard K., and Fung, Adrian K. *Microwave Remote Sensing, Active and Passive*, vol. 1. Artech House, 1981.

[12] Ulaby, Fawwaz T., Moore, Richard K., and Fung, Adrian K. *Microwave Remote Sensing, Active and Passive*, vol. 2. Artech House, 1986.

[13] Ulbrich, C. W. Natural variation in the analytical form of the raindrop-size distribution. *Journal of Climate and Applied Meteorology 22* (October 1983), 1764–1775.